

## RESEARCH ARTICLE

10.1029/2018JB015588

## Extension and Dynamics of the Andes Inferred From the 2016 Parina (Huarichancara) Earthquake

Sam Wimpenny<sup>1</sup> , Alex Copley<sup>1</sup>, Carlos Benavente<sup>2</sup> , and Enoch Aguirre<sup>2</sup> <sup>1</sup>COMET, Bullard Laboratories, Department of Earth Sciences, University of Cambridge, Cambridge, UK, <sup>2</sup>Instituto Geológico, Minero y Metalúrgico (INGEMMET), Lima, Peru

## Key Points:

- The Parina earthquake led to NE-SW extension in the high Andes of south Peru
- Faults in the South American forelands have an effective coefficient of friction less than 0.2
- The strength of faults within the forelands modulates the stress state in the high Andes

## Supporting Information:

- Supporting Information S1

## Correspondence to:

S. Wimpenny,  
sew57@cam.ac.uk

## Citation:

Wimpenny, S., Copley, A., Benavente, C., & Aguirre, E. (2018). Extension and dynamics of the Andes inferred from the 2016 Parina (Huarichancara) earthquake. *Journal of Geophysical Research: Solid Earth*, 123. <https://doi.org/10.1029/2018JB015588>

Received 1 FEB 2018

Accepted 23 AUG 2018

Accepted article online 29 AUG 2018

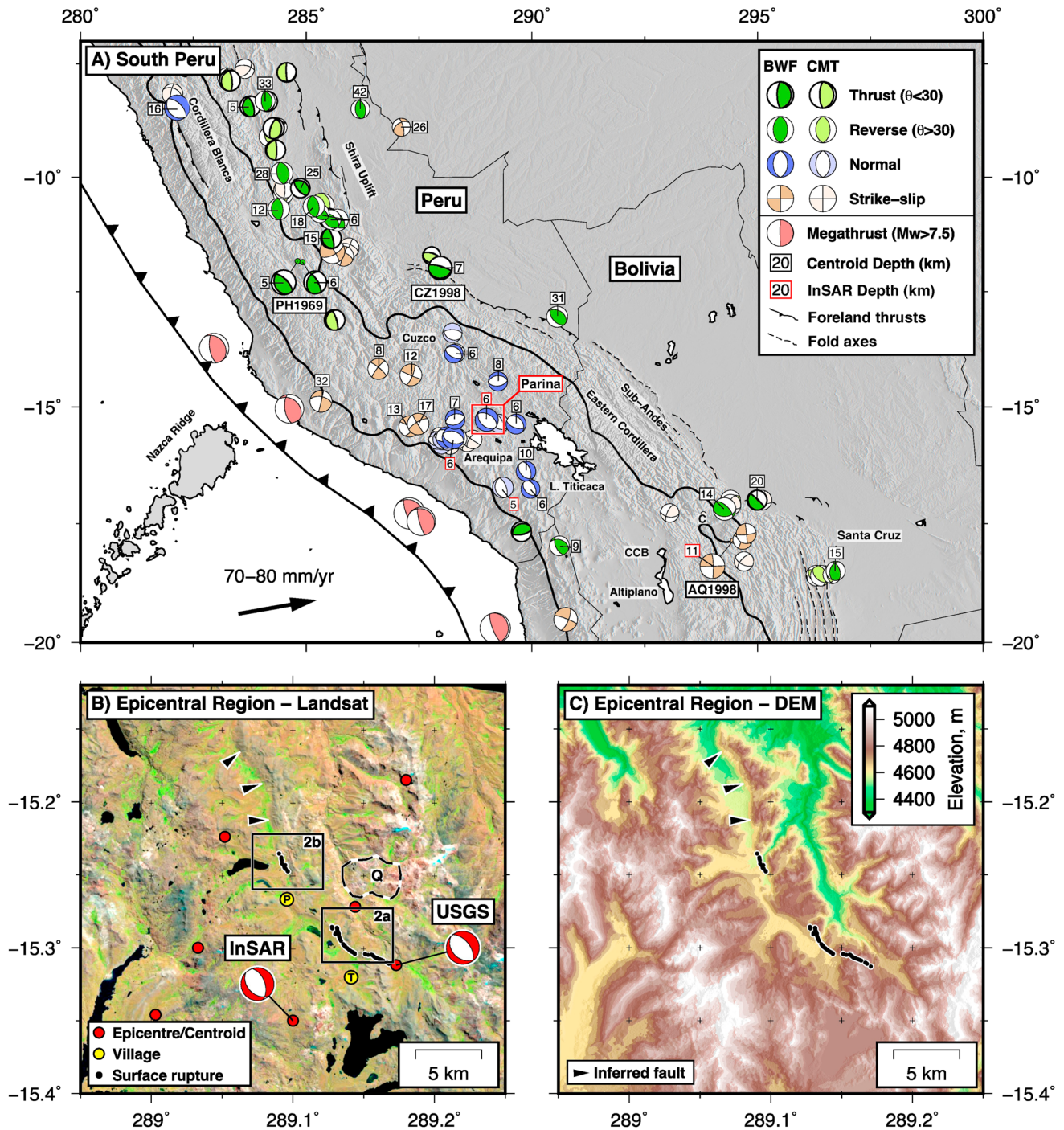
**Abstract** The  $M_w$  6.1 2016 Parina earthquake led to extension of the south Peruvian Andes along a normal fault with evidence of Holocene slip. We use interferometric synthetic aperture radar, seismology, and field mapping to determine a source model for this event and show that extension at Parina is oriented NE-SW, which is parallel to the shortening direction in the adjacent sub-Andean lowlands. In addition, we use earthquake source models and GPS data to demonstrate that shortening within the sub-Andes is parallel to topographic gradients. Both observations imply that forces resulting from spatial variations in gravitational potential energy are important in controlling the geometry of the deformation in the Andes. We calculate the horizontal forces per unit length acting between the Andes and South America due to these potential energy contrasts to be  $4\text{--}8 \times 10^{12}$  N/m along strike of the mountain range. Normal faulting at Parina implies that the Andes in south Peru have reached the maximum elevation that can be supported by the forces transmitted across the adjacent foreland, which requires that the foreland faults have an effective coefficient of friction  $\lesssim 0.2$ . Additionally, the onset of extension in parts of the central Andes following orogen-wide compression in the late Miocene suggests that there has been a change in the force balance within the mountains. We propose that shortening on weak detachment faults within the Andean foreland since  $\sim 5\text{--}9$  Ma reduced the shear tractions acting along the base of the upper crust in the eastern Andes, leading to extension in the highest parts of the range.

## 1. Introduction

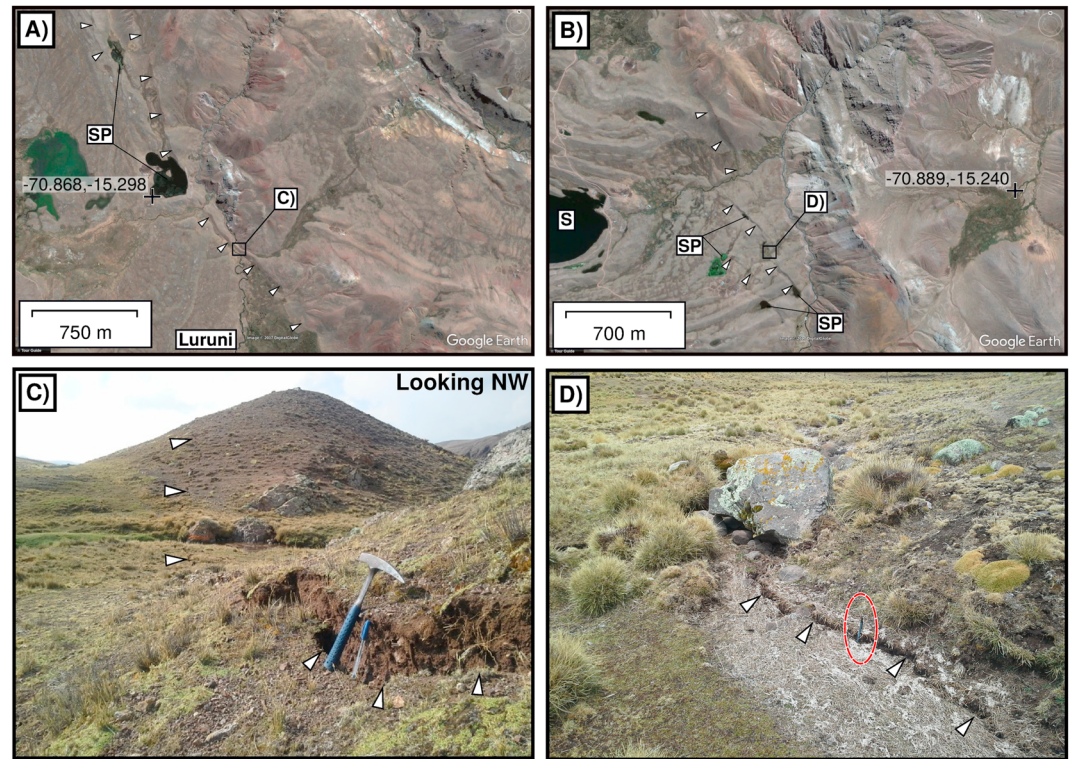
On 1 December 2016 (22:40:26 UTC) a  $M_w$  6.1 normal-faulting earthquake occurred  $\sim 70$  km west of Lake Titicaca in the south Peruvian Andes (Figure 1a). This event marks the first  $M_w > 6$  extensional earthquake to occur within the Andes for 70 years and provides a rare opportunity to study crustal deformation, lithosphere rheology and the forces driving deformation in this region.

Observations of crustal deformation within the high Andes are sparse but are fundamental to testing models of orogen dynamics (e.g., England & Houseman, 1989; Flesch & Kreemer, 2010; Liu et al., 2002). One particular area of contention is whether extension in the high Andes is parallel (e.g., Dalmayrac & Molnar, 1981) or perpendicular (e.g., Mercier et al., 1992; Sébrier et al., 1985) to shortening in the adjacent sub-Andean lowlands. Extension in the Andes parallel to shortening in the sub-Andes can be explained by the balance between the forces arising from differences in gravitational potential energy between the mountains and lowlands, and the forces acting through the foreland lithosphere (Dalmayrac & Molnar, 1981; Froidevaux & Isacks, 1984). However, if extension in the Andes is perpendicular to sub-Andean shortening, shear tractions acting on the base of the Andean lithosphere are required to influence the stress state in the mountains (e.g., Liu et al., 2002).

Current observations of normal-faulting earthquakes in the Andes (Cabrera & Sébrier, 1998; Devlin et al., 2012; Doser, 1987; Jay et al., 2015) provide a limited constraint on the geometry of the extension, as the majority of the events are too small ( $M_w < 5.5$ ) to break the full thickness of the seismogenic layer, so may not be representative of the dominant crustal strain (e.g., Brune, 1968; Jackson & Blenkinsop, 1997; Jackson & White, 1989; Scholz, 2002). To supplement the sparse earthquake data, a number of studies have inferred the direction of extension throughout the Andes to be N-S based on slip vectors along minor fault planes (e.g., Cladouhos et al., 1994; Daxberger & Riller, 2015; Mercier et al., 1992; Schoenbohm & Strecker, 2009; Sébrier et al., 1985; Tibaldi & Bonali, 2018). However, slip on minor faults also represents a small component of the total crustal strain and may not accurately record the bulk orientation of extension (Riller et al., 2017).



**Figure 1.** Overview of the Parina earthquake epicentral region. Waveform modeled (BWF) and global catalogue earthquakes (gCMT; Ekström et al., 2012) with  $M_w > 5$  in the overriding plate are shown in (a) (see supporting information Table S1 for sources). We do not include earthquakes offshore in the forearc. PH1969 are the 1969 Pariahuanca earthquakes (Philip & Megard, 1977; Suarez et al., 1983), AQ1998 is the 1998 Aiquile earthquake (Funning et al., 2005), and CZ1998 is the 1998 Cuzco foreland earthquake (Emmerson, 2007). C marks the Cochabamba and Punata basins, and CCB marks the Corque-Corococo Basin. The thick black line is the 3,000-m contour from the 100-km Gaussian-filtered topography. The red box marks the location of (b) and (c). (b) A Landsat 8 (bands 4, 3, and 2) image of the epicentral region. Black dots are the coseismic surface ruptures, and black triangles mark the inferred extension of the Parina Fault north of the surface ruptures. P and T marks the villages of Parina and Togra. The centroid and mechanism of the best fit interferometric synthetic aperture radar (InSAR) fault plane, and the epicenter of the U.S. Geological Survey (USGS) source model, are shown together with the epicenters of  $M_w > 4.0$  National Earthquake Information Center aftershocks (location error  $> 5$  km). Black boxes outline the locations of the satellite imagery in Figure 2, and the region marked Q is an open cast quarry. (c) The Shuttle Radar Topography Mission 1-arc sec topography covering the same region as (b), highlighting the NW-SE trending step in topography associated with the Parina Fault. DEM = digital elevation model.



**Figure 2.** Geomorphology and surface ruptures of the 1 December 2016 Parina earthquake. (a) A GoogleEarth satellite image (from 2015) of the southern end of the coseismic ruptures near Togra (see Figure 1b). White triangles pick out small scarps in the topography that are associated with the mapped coseismic surface ruptures, and bodies of water marked SP are small ponds dammed against the footwall scarp of the Parina Fault. (b) A similar GoogleEarth image (from 2015) over the northern end of the ruptures near Saguanani Lake (marked S). The vertical offsets across the surface ruptures in the southern section are up to 30 cm in height (c, geological hammer for scale) and have a small opening component, while at the northern end of the rupture, most of the features are hairline ruptures and have <10-cm offset (d, pen circled in red for scale).

There also exists competing views regarding the orientation of shortening across the sub-Andean lowlands. Studies of earthquakes suggest that shortening in the sub-Andes is parallel to gradients in the topography (Assumpção, 1992; Assumpção & Araujo, 1993; Lamb, 2000). Alternatively, some studies have argued that the GPS velocity field in the sub-Andes can be explained by a combination of elastic strain accumulation on the locked Peru-Chile subduction interface and slip along a detachment fault beneath the sub-Andes. These elastic models assume motion on the detachment fault beneath the sub-Andes has a slip vector parallel to relative plate motion between the Nazca plate and South America, rather than parallel to gradients in topography (Bevis et al., 2001; Chlieh et al., 2011).

In this study we use geomorphology, seismology, and interferometric synthetic aperture radar (InSAR) to determine a detailed source model of the 2016 Parina earthquake and relate the pattern of coseismic and postseismic fault slip to the surface geomorphology. We then combine our source model for the Parina earthquake with additional seismological source models, and existing GPS data, to reassess the pattern of crustal deformation in the high Andes, and its relationship with shortening in the adjacent sub-Andean lowlands. We use the pattern of deformation to test models of the forces driving deformation in the Andes and investigate the rheology of the South American lithosphere. Finally, we discuss possible causes for the onset of normal faulting in the high Andes at ~5–9 Ma and suggest a general model for the support and evolution of mountain ranges based upon the strength of faults in their forelands.

## 2. The 1 December 2016 Parina Earthquake

The  $M_w$  6.1 Parina earthquake occurred in a region of south Peru that has experienced a number of recent  $M_w$  5.0–5.8 normal-faulting earthquakes (Cabrera & Sebrier, 1998; Devlin et al., 2012; Dziewonski et al., 1981; Ekström et al., 2012; Jay et al., 2015; Figure 1a). Geomorphic evidence of recent normal faulting in the

epicentral region is scarce (e.g., Benavente et al., 2013) but has been documented further north near Cuzco (Benavente et al., 2013; Mercier et al., 1992; Sébrier et al., 1985; Suarez et al., 1983), and to the south near Arequipa (Lavenue et al., 2000). The limited geomorphic expression of normal faults in south Peru probably reflects the small amount of finite extensional strain in the high mountains ( $< 1\%$ ; Sébrier et al., 1985).

### 2.1. Local Geomorphology and Surface Ruptures

Surface ruptures associated with the Parina earthquake were mapped within 3 days of the event (Figure 1b) and consist of two NW-SE trending sections with an along-strike length of  $\sim 12$  km, a maximum height of  $\sim 30$  cm (downthrown to the SW), and maximum tensional opening of  $\sim 30$  cm (Figure 2). The ruptures coincide with a 150 m high escarpment that extends an additional 10 km NW of Parina and bounds a fluvial basin on its SW side (Figure 1c). Tensional opening across the ruptures was largest in areas where vertical offsets were also highest, which is a common feature of normal faults that steepen in the near surface (e.g. Jackson et al., 1982).

The northern section of ruptures consist of discontinuous, overlapping splays that map onto NW-SE trending, meter high scarps visible in preevent satellite imagery (Figure 2b). Both the tensional opening and vertical offsets across the ruptures in the northern section were typically  $< 10$  cm (Figure 2d). In the southern section the ruptures have both opening and vertical components up to 30 cm (Figure 2c) and form a semicontinuous trace that also coincides with a meter high scarp (Figure 2a). Dammed ponds on the downthrown (SW) side of the scarps predate the Parina earthquake (Figures 2a and 2b) and suggest that there has probably been  $\lesssim 10$ –20 m of slip on the Parina Fault since the last major glacial epoch reset the landscape in the region at  $\sim 10$ –30 ka (Clapperton, 1983; Smith et al., 2005), implying a fault slip rate  $\lesssim 1$  mm/year.

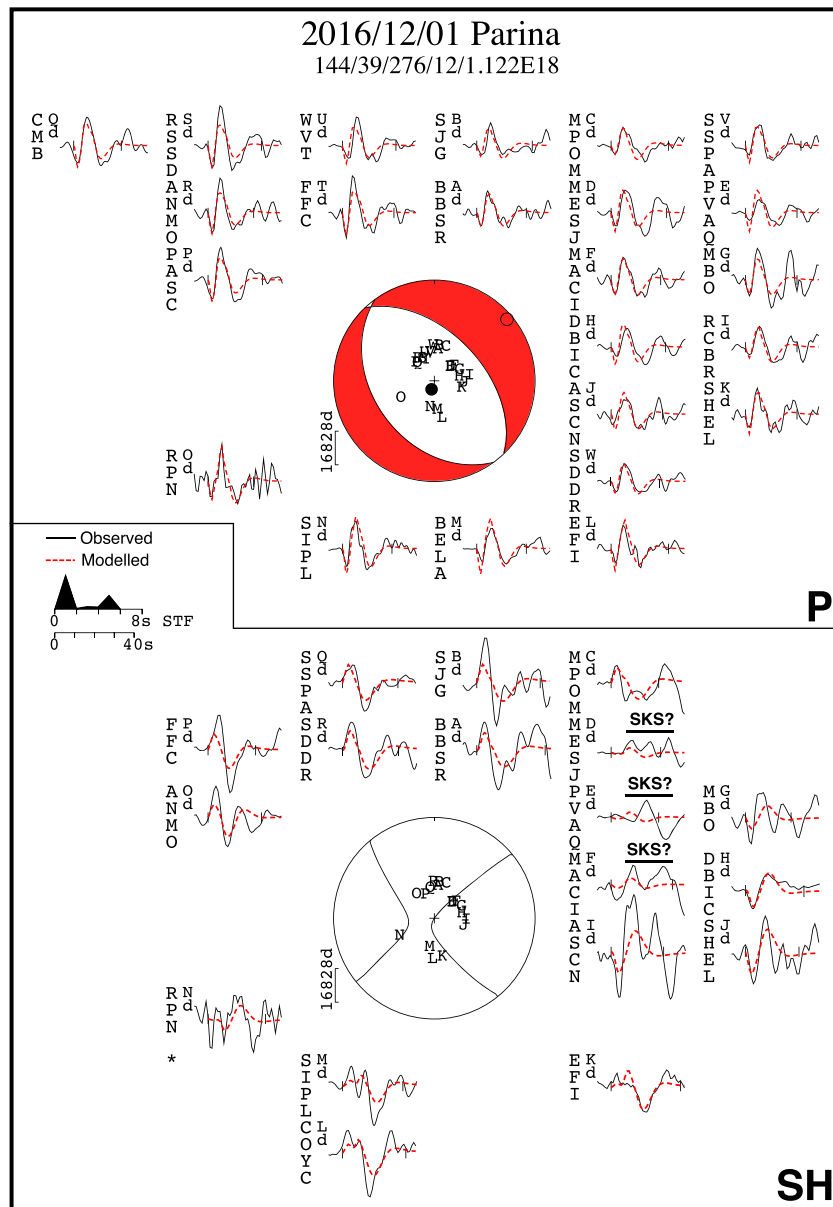
### 2.2. Teleseismic Body-Waveform Modeling

We determined the strike, dip, rake, centroid depth, source-time function, and moment release of the Parina earthquake by modeling the event as a finite-duration rupture at a point source and performing a joint inversion of long-period  $P$  and  $SH$  seismic waveforms recorded at teleseismic distances using the MT5 program of Zwick et al. (1994); based on the algorithm of McCaffrey and Abers (1988) and McCaffrey et al. (1991). The methodology behind this procedure has been described in detail elsewhere (see Molnar & Lyon-Caen, 1989; Taymaz et al., 1990); hence, only a brief summary will be provided here.

Broadband seismograms recorded at stations within  $30$ – $90^\circ$  of the earthquake epicenter were selected from the Incorporated Research Institutions for Seismology data management center and were filtered to reproduce the response of a long-period World-Wide Standardized Seismograph Network instrument (15–100 s). Long-period waveforms are insensitive to small-scale heterogeneity in the source region velocity structure (Taymaz et al., 1990); therefore, we use a simple 1-D crustal velocity model with  $V_p = 6.5$  km/s,  $V_s = 3.7$  km/s and density  $2,800$  kg/m<sup>3</sup> (Dorbath, 1996; Schurr et al., 1999). Inaccuracies in the velocity model typically lead to uncertainties in the centroid depth estimate of  $\pm 4$  km for shallow ( $< 30$  km) crustal events (Taymaz et al., 1990). Accurate arrival times of the  $P$  and  $SH$  phases were picked from the broadband seismograms. The starting model for the inversion was taken as the best double-couple gCMT solution (Ekström et al., 2012), and the final model is constrained to have a double-couple moment tensor.

The minimum-misfit solution consists of a normal-fault source with a strike/dip/rake of  $144/39/276$ , a centroid depth of 12 km, and a seismic moment of  $1.1 \times 10^{18}$  N m ( $M_w$  6.0; Figure 3). The mapped surface ruptures trend parallel to the minimum-misfit strike estimate, and the sense of motion across them indicates the SW dipping nodal plane is the fault plane.

Uncertainties in the source model were estimated by fixing each parameter of interest at values away from their best fit and performing inversions in which all other parameters were free to vary. We estimate the strike to be constrained between  $110^\circ$  and  $160^\circ$  by the deterioration in fit between  $SH$  waveforms recorded at stations DBIC, COYC, and EFI outside this range (Figure 4). Within this range of possible strikes, the dip cannot be lower than  $35^\circ$ , otherwise the stations MPOM and SJG would lie near the  $P$  wave nodal plane, and the amplitude of the predicted  $P$  arrivals would be too low to fit the observations. Mechanisms with dips  $> 55^\circ$  do not fit the observed waveforms as they predict the incorrect  $SH$  first motion at stations FFC and SSPA. The rake must be in the range  $250$ – $300^\circ$  to fit the  $SH$  first motions and amplitudes at stations DBIC, COYC, EFI, and MESJ (Figure 4). All the models that fit the observed waveforms have a slip vector azimuth between  $211^\circ$  and  $245^\circ$  (NE-SW). Centroid depths greater than 20 km cannot match the observed  $SH$  waveforms as the direct  $S$  and reflected  $sS$  phases separate, which is not observed (e.g., see clear waveform misfits at stations EFI and

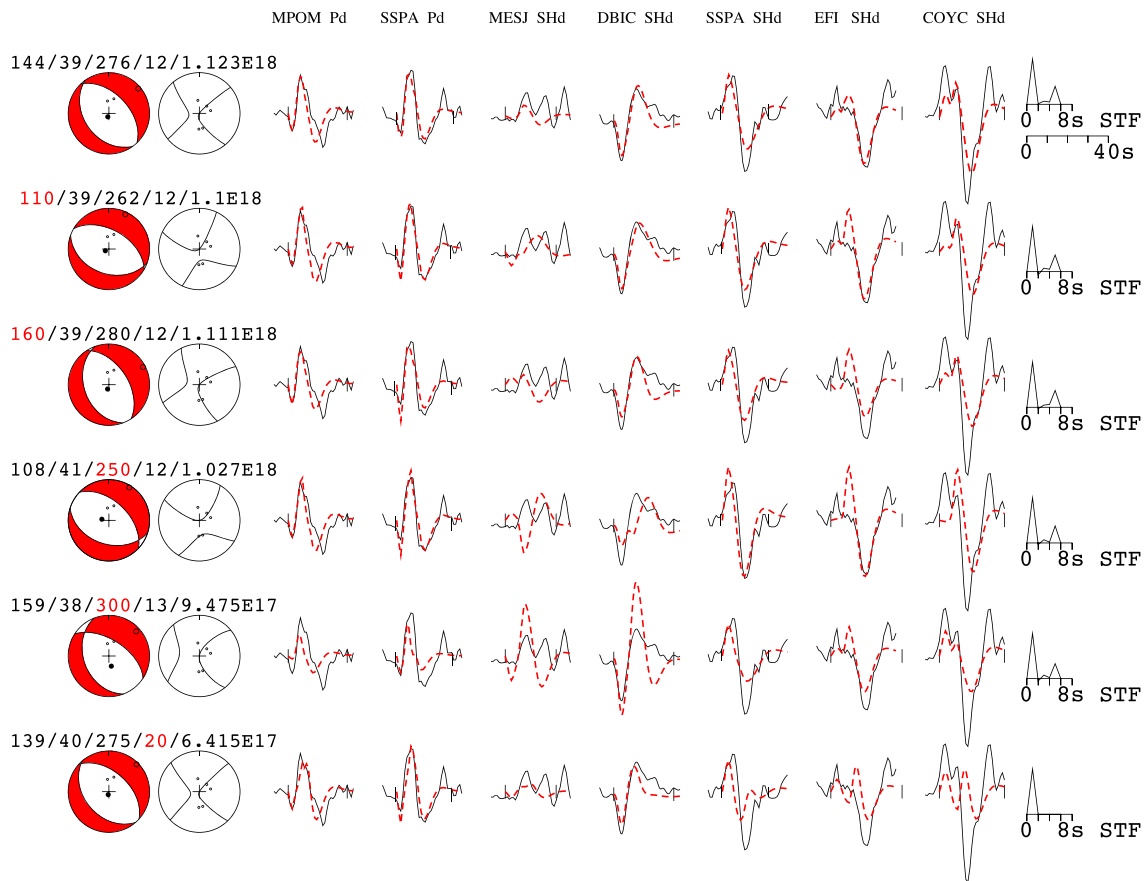


**Figure 3.** Minimum-misfit teleseismic body-waveform solution for the 1 December 2016 Parina earthquake. Details of the inversion result are shown below the title with the form strike/dip/rake/depth/moment, where depth is in kilometers and moment is in Newton meter. The top panel shows a lower hemisphere projection of the *P* wave nodal planes, with the station distribution used in the best fit inversion shown as capital letters. Observed and modeled seismograms are 40-s time series and are shown as black and red dashed lines, respectively. The seismogram station code is shown to the left of the corresponding seismogram, and the inversion time window is demarcated by vertical black ticks. *P* and *T* axes are projected onto the focal sphere as a black filled circle and an open circle, respectively. The lower panel shows the equivalent for the *SH* waves. Seismograms that are labeled with SKS occur within the 80–85° range from the epicenter, therefore may contain some signal from phases that have interacted with the core. Stations with an asterisk are weighted to 0 in the inversion as they contain a large component of noise but are included for comparison with the model predictions. The source-time function is shown as black triangles.

COYC in Figure 4). For all inversion results with a good fit to the observed waveforms, the seismic moment is  $0.9\text{--}1.4 \times 10^{18}$  N m ( $M_w$  5.9–6.1).

### 2.3. Coseismic InSAR: Observations

We formed Sentinel-1 ascending- and descending-track interferograms covering the coseismic period of the Parina earthquake using the European Space Agency's SNAP software (<http://step.esa.int/main/>). The effect of



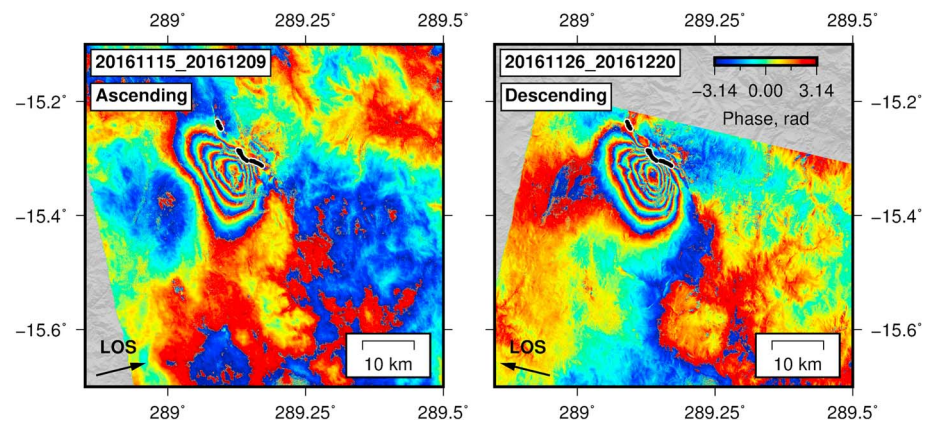
**Figure 4.** Sensitivity tests showing fits between selected waveforms of the 2016 Parina earthquake given variations in the source parameters. Each line shows *P* and *SH* focal spheres, the fault parameters in strike/dip/rake/centroid depth/moment formation, the fit between modeled (red dashed) and observed (black solid) waveforms at a set of stations, and the source-time function for that particular model. The station codes are given at the top in each column, where Pd are vertical component waveforms and SHd are transverse waveforms. The best fit model presented in Figure 3 is shown on the top row, and each subsequent row shows different inversion results in which the parameter in red is held fixed, while all other parameters can vary.

topography on phase in the interferograms was removed using a Shuttle Radar Topography Mission (SRTM) 3-arc sec elevation model (Farr et al., 2007), following which we phase filtered the interferograms (Goldstein et al., 1988) and unwrapped using the statistical-cost network-flow algorithm of Chen and Zebker (2001). Additional information about the interferograms is provided in Table S3 in the supporting information.

The wrapped interferograms (Figure 5) show 5–6 concentric, elongate fringes (corresponding to a maximum of ~15 cm of line-of-sight, LOS, displacement) oriented approximately NW-SE in both the ascending and descending track, which is consistent with ground motion resulting from a fault with the same geometry as our body-waveform solution. In addition, the similar pattern of displacement in the ascending and descending tracks implies that the majority of the deformation was vertical, which is consistent with motion on a dip-slip fault (e.g., Copley et al., 2015). The smooth fringe pattern, located to the SW of the surface ruptures, and the higher fringe density in the NE than the SW of the displacement patch, implies that the majority of slip remained buried on a fault that dips SW and has an updip projection coincident with the surface ruptures. The along-strike width of the fringes is ~15 km, and faults that are ~15 km long typically produce  $M_w$  6.0–6.5 earthquakes (Wells & Coppersmith, 1994).

#### 2.4. Coseismic InSAR: Modeling

We determine the source parameters of the fault responsible for the 2016 Parina earthquake by inverting the InSAR measurements of surface displacement for the best fitting constant-slip, rectangular, elastic dislocation (Okada, 1985) using a simulated annealing algorithm that minimizes the root-mean-square (RMS) misfit between model and observations (e.g., Copley et al., 2015). We solve for the location of the fault plane, its length, width, strike, dip, rake, the amount of slip, and a constant offset and linear ramp in LOS across



**Figure 5.** Wrapped coseismic interferograms covering the 1 December 2016 Parina earthquake. The dates of the preevent and postevent acquisitions are given in the form YYYYMMDD, and the line-of-sight vector is shown in the bottom left. The incidence angle of this vector relative to the Earth's surface is between 30–43°. Black dots outline the locations of the coseismic surface ruptures.

each interferogram to account for long-wavelength atmospheric and orbital artifacts. The interferograms are downsampled uniformly over the inversion window to 200×200-m pixels to reduce the number of data points in the inversion to ~70,000. The starting model for the inversion is taken to be the SW dipping nodal plane of our minimum-misfit body-waveform solution.

To assess the fit between the models and the observations, we estimate the noise levels in the interferograms using the magnitude of phase variations within nondeforming regions. Noise in the interferograms leads to apparent LOS variations between 1.0 and 1.1 cm in the ascending interferogram, and between 0.8 and 0.9 cm in the descending interferogram.

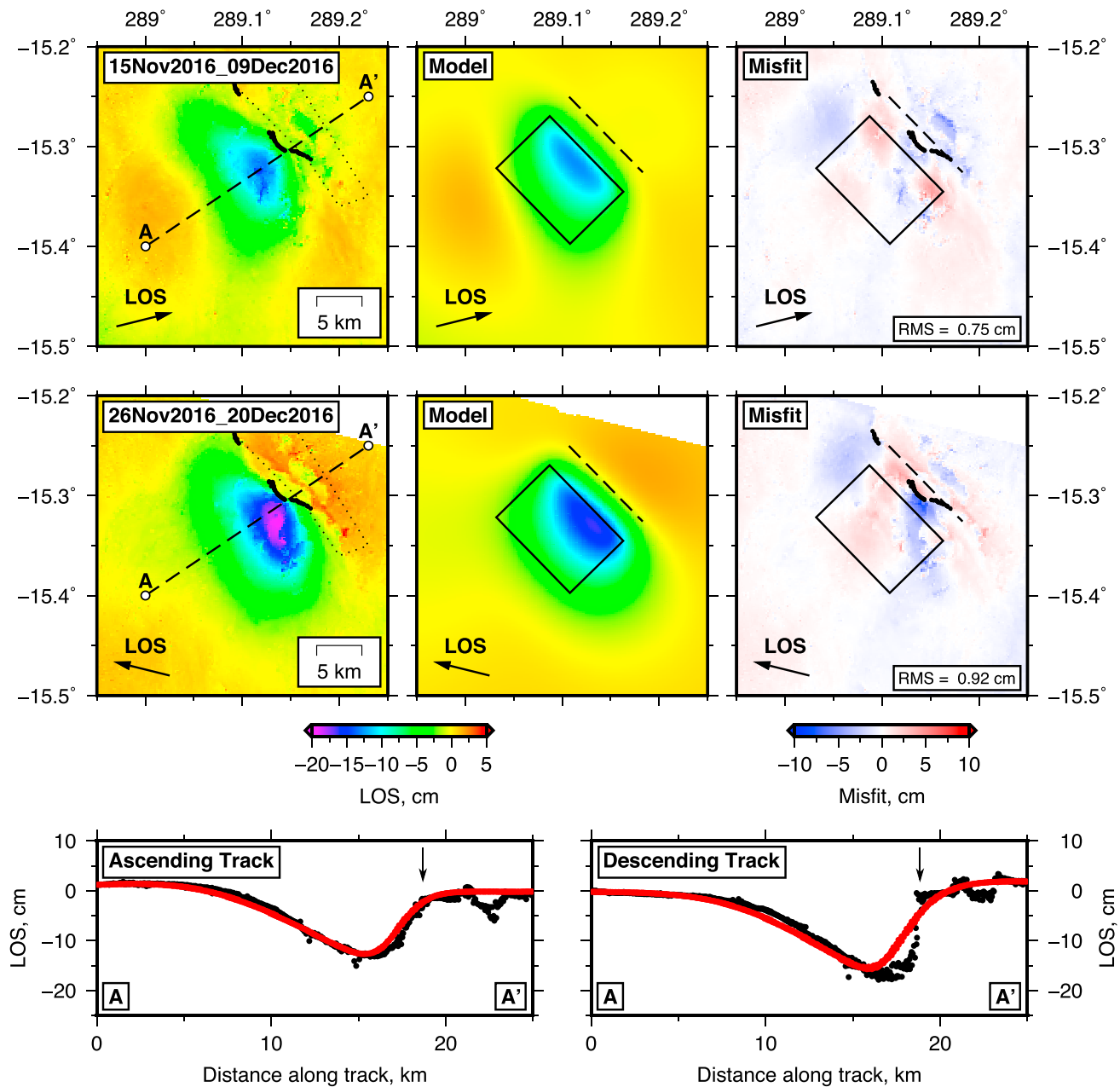
The inversion results suggest that the InSAR data are best fit by ~0.5 m of slip buried on a 13-km-long normal fault with a strike/dip/rake of 135/40/250 that mostly ruptured between 3- and 10-km depth (Figure 6). The surface projection of the best fit fault plane is coincident with the surface ruptures. RMS residuals between the best fit model and the InSAR observations are 0.8 cm for the ascending track and 0.9 cm for the descending track; therefore, the data are fit to within the noise levels, and a more complex model of distributed fault slip is not required or justified by the data.

To test the sensitivity of the InSAR measurements to changes in the fault geometry, we performed a grid search of inversions in which each fault parameter was independently fixed at a range of values, while all others could vary, and measured how the misfit evolved (Figure 7). We find that fault planes with strike = 120–145°, dip = 35–55°, rake = 250–270°, top depth = 1.5–4.5 km, and bottom depth = 6–14 km can match the InSAR observations to within the noise levels. Together the range of acceptable solutions allows the slip vector azimuth to be between 230° and 280° (Figure 7). The teleseismic waveform modeling constrains the slip vector azimuth to be between 211° and 245°; therefore, the range of slip vectors consistent with all of the InSAR, seismology, and surface rupture constraints have an azimuth of 230–245° (NE-SW; see Figure 7).

### 2.5. Postseismic Deformation

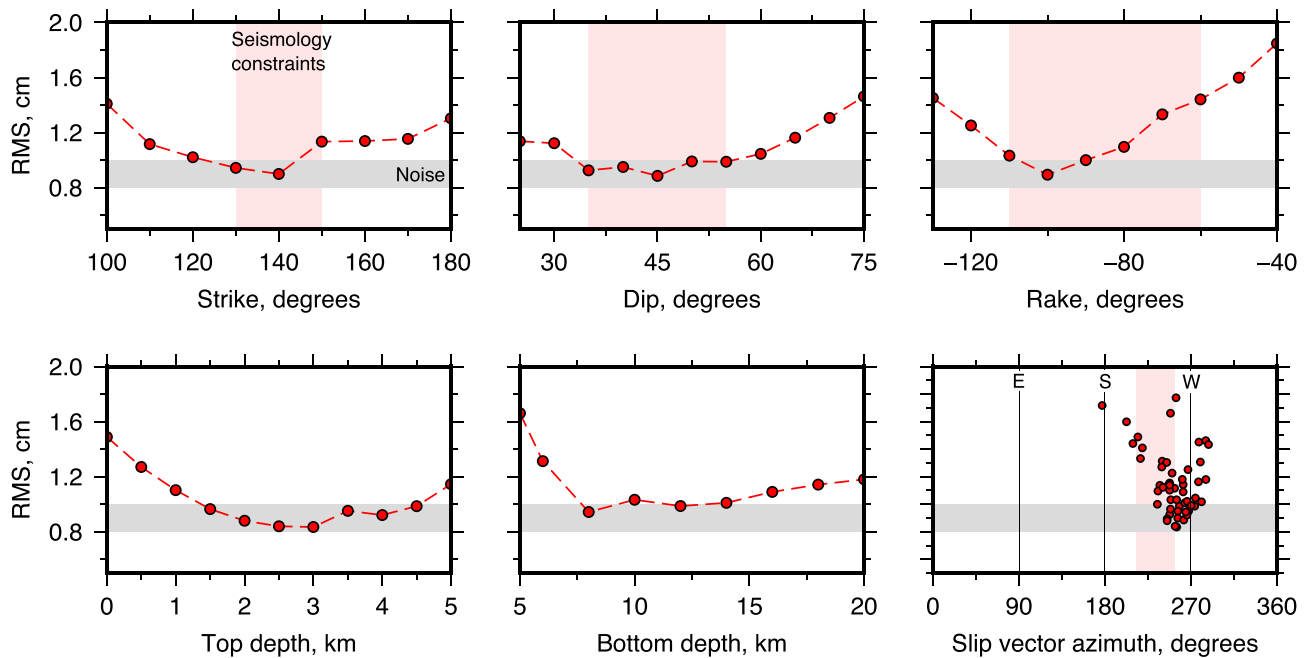
Models of coseismic fault motion indicate that the majority of slip in the Parina earthquake remained buried below 3-km depth (Figures 6 and 7). However, the 10- to 30-cm-high surface ruptures measured 3 days after the earthquake suggest that some coseismic slip reached the surface. Decreasing coseismic slip on faults at shallow depths is common (e.g., Fialko et al., 2005) and has previously been observed for normal faults (e.g. Bie et al., 2014; Copley, 2012). Limited shallow coseismic slip is likely to reflect either inelastic deformation of the near-surface (Kaneko & Fialko, 2011), rate-strengthening frictional properties of the shallow fault zone (Marone & Scholz, 1988; Scholz, 1998), or both. In the latter case, the fault may creep postseismically (*afterslip*), causing transient, short-wavelength surface deformation near the coseismic rupture.

We formed interferograms covering the first 8 months following the Parina earthquake (Figure 8a). In addition, we also generated a time series of postseismic deformation by extracting the relative LOS motions to either



**Figure 6.** Results of inversions for the best fitting elastic dislocation model to the observed interferometric synthetic aperture radar surface displacements. The left panels show the unwrapped and downsampled interferograms covering the coseismic period. We use the convention that +ve line of sight (LOS) is motion toward the satellite. The black polygon delineates a region with short wavelength, spatially variable LOS displacements that are likely to represent offsets at the surface generated by local slope failure in the steep valley NE of Parina, and open cast quarrying activity (Figure 1b). The black dots are the mapped coseismic surface ruptures. The best fitting model is shown in the middle panels, with the map view of the fault plane shown as a black rectangle, and its surface projection as a black dashed line. The misfit between the observations and models is shown in the panels on the right. Profiles between A-A' through the observations (black dots) and models (red dots) are shown below. Steep gradients of LOS displacement near the surface ruptures (shown by the vertical arrows) are clear in the descending-track profile, however are not present in the smoother ascending-track data. These differences between the surface displacement may reflect postseismic afterslip, as the descending-track acquisition was collected 19 days after the earthquake, while the ascending-track data only includes 8 days of postseismic deformation. We present models and a discussion of the postseismic deformation in section 2.5.





**Figure 7.** Sensitivity analysis of the interferometric synthetic aperture radar inversions to the fault parameters. The light red bars mark the possible range of fault parameters determined from the seismological body-waveform modeling (Figures 3 and 4) and the orientation of the surface ruptures. The grey bar shows the noise levels in the interferograms. The slip vector azimuth is given as the motion of the footwall relative to the hanging wall in degrees clockwise from north. RMS = root-mean-square.

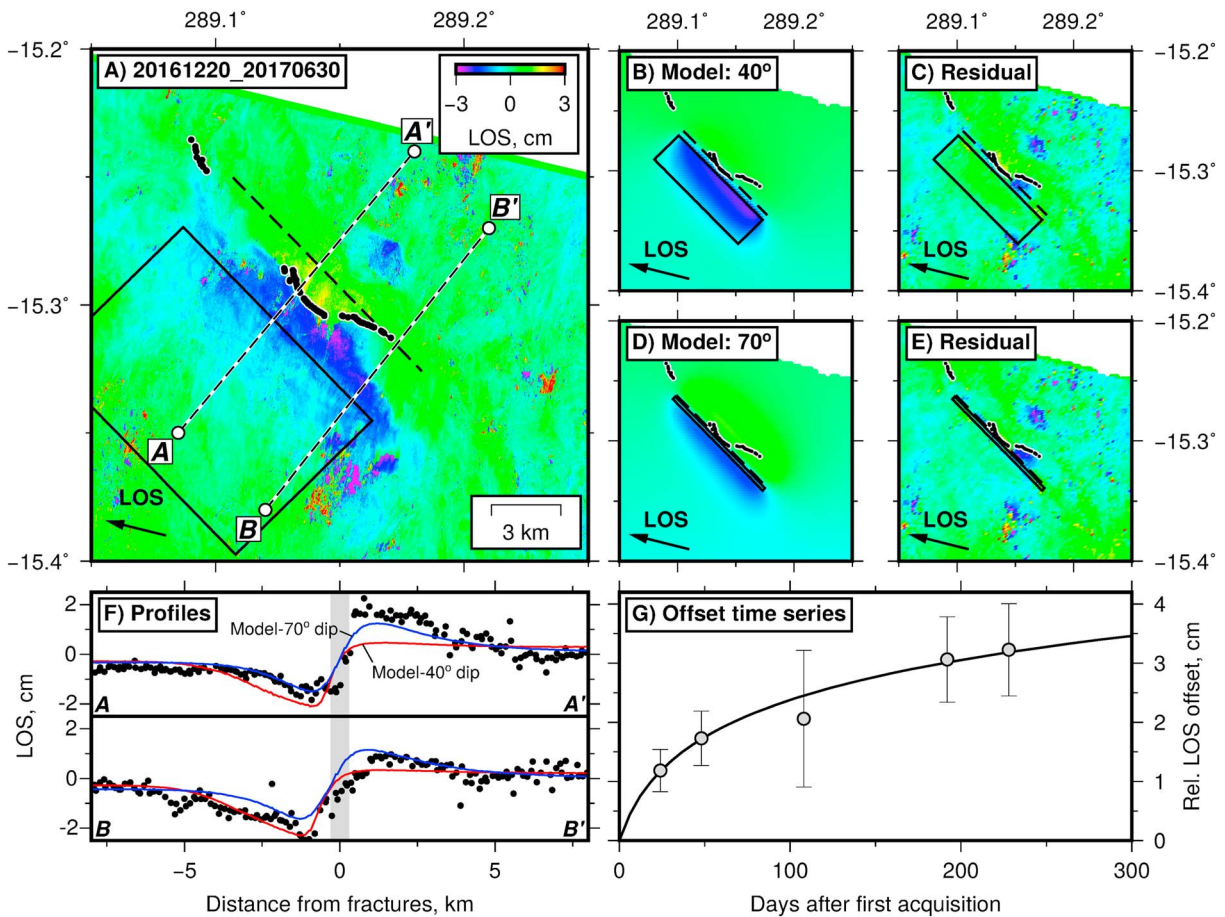
side of the surface ruptures from a series of interferograms that were formed with a common postearthquake acquisition (collected within 19 days of the earthquake) as the reference image in each pair.

The descending-track interferograms reveal a sharp offset in the LOS displacement field across the central section of surface ruptures, with the size of the offset increasing with time after the earthquake (Figures 8a and 8f). The LOS offset decays with distance perpendicular to the surface ruptures over a length scale of  $\sim 3\text{--}5$  km (Figure 8f), indicating that the majority of postseismic deformation is within the top 5 km of the crust. Postseismic signals are less clear in the ascending-track interferograms due to the larger component of atmospheric noise (supporting information Figure S14). The temporal evolution of the postseismic deformation follows a typical logarithmic transient decay (e.g., Ingleby & Wright, 2017; Smith & Wyss, 1968) with a relaxation time of 12 days (Figure 8g), which is similar to estimates from a number of other studies (e.g., Fielding et al., 2009; Savage et al., 2005).

We interpret the postseismic InSAR observations to reflect shallow afterslip on the updip extension of the coseismic fault plane, and not shallow poroelastic deformation (e.g., Fielding et al., 2009; Peltzer et al., 1998), because the sharp step in LOS directly correlates with the location of the coseismic surface ruptures, and the polarity of the LOS motions are the same as those in the earthquake. We inverted the observed surface displacements 6 months after the Parina earthquake for the best fit, constant-slip fault (as in section 2.4) with the rake fixed to that of the coseismic fault model. The postseismic InSAR measurements are consistent with  $\sim 6\text{--}7$  cm of afterslip on a fault with equivalent strike, dip, and length to the coseismic fault plane, but with afterslip focused between 0- and 4-km depth (Figures 8b and 8d). However, the constant-slip model cannot match both the smooth LOS displacement pattern south of the surface ruptures, and the sharp change in LOS across the central section of the ruptures (Figures 8a and 8f), indicating that afterslip did not extend to the surface along the whole fault. In addition, a small region of symmetrical footwall uplift and hanging wall subsidence across the southern section of surface ruptures requires a locally steeper dipping fault plane of  $\sim 70^\circ$  to fit the observed LOS motion in that area (Figures 8a and 8f).

## 2.6. Parina Earthquake: Summary

We find that the Parina earthquake ruptured a 13-km-long, NW-SE trending, SW dipping, shallow-crustal normal fault with a NE-SW ( $230\text{--}245^\circ$ ) oriented slip vector azimuth (source models summarized in Table 1). The majority of slip in the earthquake ( $\sim 0.5$  m) was buried between 3- and 10-km depth; however, a small



**Figure 8.** Postseismic deformation following the 2016 Parina earthquake. (a) A descending-track interferogram covering 6 months of postseismic deformation with a linear, long-wavelength ramp removed. The preevent and postevent acquisition dates are given in YYYYMMDD format in the top left, and the black dots are the coseismic surface ruptures. The map view of the best fit coseismic fault plane is shown as a black solid line, and its surface projection as a black dashed line. (b) The best fit fault model to the postseismic surface displacement when the fault strike, dip, and rake are fixed to the coseismic fault plane. (c) The residual between the model prediction and the observed surface displacement. (d and e) The best fit fault model when the strike and rake are fixed to their coseismic values, and the dip is fixed to 70°. Profiles through the deformation field between A-A' and B-B' are shown in (f), where the black dots are the observed line-of-sight (LOS) changes, the red lines are the model in (b), the blue lines are the model in (d), and the grey bar denotes the location of the surface ruptures. The temporal evolution of deformation in (g) records the change in relative LOS between the immediate hanging wall and footwall of the Parina Fault derived from a series of interferograms with a common reference. Error bars are the 1 standard deviation bounds on the difference in LOS offset between the immediate hanging wall and footwall of the fault. The black solid line is a best fit curve of the form  $a \ln(1 + t/t_r)$ , showing that the postseismic deformation decays with the logarithm of elapsed time (e.g., Fielding et al., 2009; Savage et al., 2005; Smith & Wyss, 1968).

component of slip did extend to the surface (0.1–0.3 m). Within 6 months of the earthquake around 15–35% of the shallow coseismic slip deficit was released through postseismic afterslip updip of the coseismic rupture.

Only by combining geodetic, seismological, and field observations have we been able to properly quantify the uncertainty in the earthquake slip vector and show that the direction of extension at Parina is NE-SW. Seismicity surrounding Parina is typically confined to the top 10–15 km of the crust (Figure 1a), suggesting that the Parina earthquake ruptured most, if not all, of the seismogenic layer. As a result, the NE-SW extension is likely to be representative of the dominant strain within this region.

Shortening in the adjacent sub-Andean lowlands recorded in earthquake slip vectors and the orientation of fold axes and thrust fault scarps is parallel to the direction of extension at Parina (Figure 1a), implying that the mountains are locally deforming in plane strain. Smaller normal-faulting earthquakes with poorly constrained source parameters show a similar pattern, but with significant variability, in which the direction of extension appears to be roughly oriented (within  $\pm 45^\circ$ ) with shortening in the adjacent sub-Andes (Cabrera & Sebrier, 1998; Devlin et al., 2012; Jay et al., 2015). This is the pattern of fault slip expected if deformation within a

**Table 1**

Comparison of the Source Parameters Determined From the Surface Ruptures, Seismology, and InSAR Observations of the Parina Earthquake

Method	Strike	Dip	Rake	<i>L</i> (km)	<i>W</i> (km)	$\bar{u}$ (m)	$M_0$ (N m)
gCMT	148°	43°	274°	—	—	0.4 <sup>a</sup>	2.2×10 <sup>18</sup>
USGS	134°	35°	263°	—	—	0.5 <sup>a</sup>	2.3×10 <sup>18</sup>
Ruptures	130–145°	—	—	12	—	0.1–0.3	0.4–1.3×10 <sup>18</sup> <sup>b</sup>
BWF	144° (110–160°)	39° (30–55°)	276° (250–300°)	—	—	0.2 <sup>a</sup>	0.8–1.4×10 <sup>18</sup>
InSAR	135° (120–145°)	40° (35–55°)	250° (250–270°)	13	12	0.5	2.4×10 <sup>18</sup>

Note. BWF indicates the long-period body-waveform solution. *L* and *W* are the along-strike length and downdip width of the rupture patch, respectively. Moment is calculated using  $M_0 = \mu A \bar{u}$ , where  $\mu$  is the shear modulus (30 GPa), *A* is the fault area and  $\bar{u}$  is the average fault slip. For the body-waveform and InSAR model the range of acceptable fault geometry parameters is given in brackets next to the best fit value. InSAR = interferometric synthetic aperture radar; USGS = U.S. Geological Survey. <sup>a</sup>Values have been calculated assuming the fault is 13 km long and square. <sup>b</sup>Values have been calculated assuming the fault rupture is square (i.e.,  $L \approx W$ ).

mountain range is controlled by a contrast in gravitational potential energy between the mountains and its surrounding lowlands (e.g., Copley et al., 2009; Dalmayrac & Molnar, 1981).












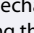
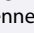
In the next section we assess the extent to which potential energy contrasts control the deformation patterns in the Andes and the South American forelands, using well-constrained depths and mechanisms of recent moderate-to-large magnitude earthquakes and existing GPS measurements.

### 3. Dynamics of Deformation in the Andes

The forces controlling deformation in mountain ranges derive predominantly from (1) relative motions of the bounding plates, (2) gravity acting on density contrasts within the lithosphere, and (3) shear tractions on the base of the overriding lithosphere from the underthrusting of rigid foreland material (Artyushkov, 1973; Copley, Avouac, & Wernicke, 2011; England & Houseman, 1989; Wdowinski et al., 1989). These forces are in a quasi-static balance with each other, viscous resistance within the ductile lithosphere, and shear resistance on faults within the brittle crust. Different contributions of these forces to the overall balance will be reflected in the pattern of active faulting within the mountain range and its forelands (e.g., Molnar & Lyon-Caen, 1988).

**Table 2**

Waveform Modeling Results for Earthquakes in South America (Not Including Parina; See Table 1)

Date (YYYY MM DD)	Time (GMT)	Longitude (°)	Latitude (°)	<i>s/d/r</i>	$M_w$	<i>z</i> (km)	% DC	Mech
1993 07 22	04:57:15	−71.18	6.49	024/35/−93	6.4	18	—	 , b
1994 05 31	17:42:04	−72.04	7.39	138/38/78	6.1	6	—	 , b
1995 01 19	15:05:11	−72.94	5.04	214/57/97	6.5	21	—	 , b
1995 10 03	01:51:37	−77.53	−2.55	216/40/103	6.8	19	—	 , b
2001 06 29	22:30:21	−70.35	−15.37	110/58/−107	5.4	6	82	 , a
2001 08 12	00:16:32	−70.03	−16.76	130/45/−108	5.1	6	87	 , a
2006 08 09	22:36:11	−70.75	−14.45	082/51/−93	5.2	8	87	 , a
2009 11 06	08:50:02	−64.46	−23.44	224/30/131	5.4	20	92	 , a
2010 02 27	15:45:43	−65.76	−24.85	162/25/97	6.2	9	99	 , B
2011 10 06	11:12:37	−64.22	−24.18	176/56/91	5.9	15	—	 , b
2014 02 17	09:41:40	−71.58	6.64	008/67/117	5.3	28	70	 , a
2015 11 29	18:52:59	−64.65	−23.56	222/29/129	5.8	4	98	 , B
2017 04 18	17:49:59	−75.31	−2.73	028/42/88	5.9	15	88	 , B

Note. % DC is the percentage double-couple of the gCMT moment tensor (as defined in Jackson et al., 2002). Mechanisms with reference *a* are modeled by fitting vertical component seismograms with synthetic waveforms following the methods of Maggi, Jackson, Priestley, and Baker (2000) and Craig et al. (2012) based on Chapman (1978) and Kennett et al. (1995) (see supporting information), while those with reference *b* are modeled using long-period body-waveform inversion. For events labeled *B* we fixed the earthquake mechanism and inverted for depth, source-time function and moment only.

In order to investigate the pattern of active faulting in the Andes and South America, we compiled a catalogue of earthquakes with  $M_w > 5$  that have been modeled using body waveforms or  $P$  wave first motions from literature sources (Alvarado & Beck, 2006; Assumpção, 1992; Assumpção & Araujo, 1993; Assumpção & Suarez, 1988; Chinn & Isacks, 1983; Devlin et al., 2012; Doser, 1987; Emmerson, 2007; Kadinsky-Cade et al., 1985; Scott et al., 2014; Suarez et al., 1983; Tavera & Buform, 2001; Vega & Buform, 1991) and 13 new solutions of our own (shown in Table 2). In addition, we included well-constrained gCMT catalogue events with >80% double-couple moment tensors (as defined in Jackson et al., 2002) from Dziewonski et al. (1981) and Ekström et al. (2012), with hypocentral depths taken from the catalogue of Engdahl et al. (1998) where available. We have included waveform-modeled earthquakes with  $M_w$  5.0–5.5 in this compilation, as small earthquakes provide information on the depth extent of faulting in South America (e.g., Assumpção, 1992; Assumpção & Suarez, 1988; Devlin et al., 2012). Below we describe the pattern of earthquakes, in conjunction with GPS and geomorphological information, and discuss the implications for the forces acting on the Andes and the South American foreland.

### 3.1. Faulting in the High Andes

Moderate-magnitude earthquakes in the crust of the high Andes are infrequent but reveal a pattern of predominantly shallow (<10–15 km) normal and strike-slip faulting events (Cabrera & Sebrier, 1998; Devlin et al., 2012; Doser, 1987; Holtkamp et al., 2011; Jay et al., 2015; this study; Figure 1a). One exception to this pattern is seen adjacent to the Shira Uplift in south Peru, where oblique reverse faulting in the high Andes was observed in the 1969 Pariahuanca earthquakes (Philip & Megard, 1977; Sébrier et al., 1988; Suarez et al., 1983; see PH1969; Figure 1a). Otherwise the majority of the reverse-faulting earthquakes are confined to regions <3,000-m elevation (Suarez et al., 1983). The dependence of faulting mechanism on elevation is typical of mountain ranges in which gravitational potential energy contrasts are an important factor in the forces controlling deformation (Copley et al., 2009; Dalmayrac & Molnar, 1981).

Nearly all of the moment release from recent normal-faulting seismicity in the high Andes has been focused in south Peru, while the Altiplano and Puna plateau have remained essentially aseismic over the same time period (Figure 1a). Geomorphological evidence of recent normal faulting is also concentrated in south Peru, with a number of studies identifying meter high Holocene fault scarps bounding footwall uplifts with a few hundred meters of relief (e.g., Sangarara Fault (Suarez et al., 1983); Tambomachay Fault (Mercier et al., 1992); Langui-Layo Fault (Benavente et al., 2013); Parina Fault (This study)). GPS measurements in south Peru limit the cumulative NE-SW extension rate across the high Andes to <5 mm/year (Kendrick et al., 2001; Villegas-Lanza et al., 2016), which is equivalent to an extensional strain rate <  $2 \times 10^{-8}$  year<sup>-1</sup> over the 250-km-wide plateau. In contrast, there is no evidence of recent fault-controlled relief in the Bolivian Altiplano, and the shallow crust is inferred to be undeforming (Lamb, 2000; Lamb & Hoke, 1997; Weiss et al., 2016). Schoenbohm and Strecker (2009) and Zhou et al. (2013) identified a number of putative normal faults within the Puna plateau; however, few of those mapped were associated with Holocene surface ruptures, and their estimated slip rates are  $\lesssim 0.1$  mm/year over the last 0.5 Myr. Therefore, both the recent seismicity and Holocene fault activity imply that the high Andes in south Peru is extending faster than the Altiplano, and possibly faster than the Puna plateau.

Differences in strain rate within an isostatically compensated mountain belt deforming in response to variations in gravitational potential energy are related to differences in elevation (D'Agostino et al., 2014; England & Houseman, 1989). Crustal thickness estimates (Assumpção et al., 2013) and small (<50 mGal) free-air gravity anomalies in the central Andean plateau both suggest that elevation contrasts on length scales much larger than the elastic thickness of the Andean crust ( $T_e \approx 10$  km; Rodríguez Tribaldos et al., 2017) are predominantly isostatically supported. We isolated the long-wavelength, isostatically compensated component of the topography by filtering the SRTM 3-arc sec elevation model (Farr et al., 2007) using a Gaussian filter with a width of 100 km (i.e.,  $\gg T_e$ ). We find that the recent normal-faulting seismicity in south Peru occurs in a region with the highest smoothed modal elevation in the whole Andes at  $\sim 4,500$  m, while the Altiplano and Puna have lower modal elevations of  $\sim 3,800$  and  $\sim 4,200$  m, respectively (supporting information Figure S15). Therefore, the distribution of recent normal-faulting earthquakes may reflect higher extensional strain rates in the south Peruvian Andes compared to the surrounding mountains due to the region's high relative elevation (e.g., England & Molnar, 1997).

The current elevation contrasts influencing the extension rates within the Andes will decay exponentially via flow of the lithosphere on a timescale that is dependent its viscosity. Using the undeforming Bolivian Altiplano

as a reference, we can combine the current maximum extensional strain rate estimate in south Peru, and the current elevation contrast between south Peru and Bolivia, to compute a lower bound on the vertically averaged Newtonian viscosity of the lithosphere ( $\eta > 3 \times 10^{21}$  Pa s; see Appendix A). Assuming the forces acting on the Andes have remained constant in the late Cenozoic, and given our lower bound on the lithosphere viscosity, elevation contrasts between south Peru and the surrounding high Andes will decay with a time constant of at least  $\sim 3$  Myr and are unlikely to have existed much earlier than 10 Ma (see Appendix A).

Strike-slip faulting in the high Andes SW of Cuzco occurs where there are significant along-strike changes in the geometry of the mountain belt and the amount of E-W shortening across the sub-Andes (Kley & Monaldi, 1998; Figure 1a). In these isolated regions the Andes does not behave in a two-dimensional manner, as there is a component of strain along strike, and therefore, balancing forces on cross sections perpendicular to the range front is not appropriate. In this study we focus on regions where extension in the high Andes is parallel to shortening in the adjacent lowlands, so the forces acting on the mountain belt can be treated in two dimensions (Dalmayrac & Molnar, 1981).

### 3.2. Faulting in the Eastern Cordillera

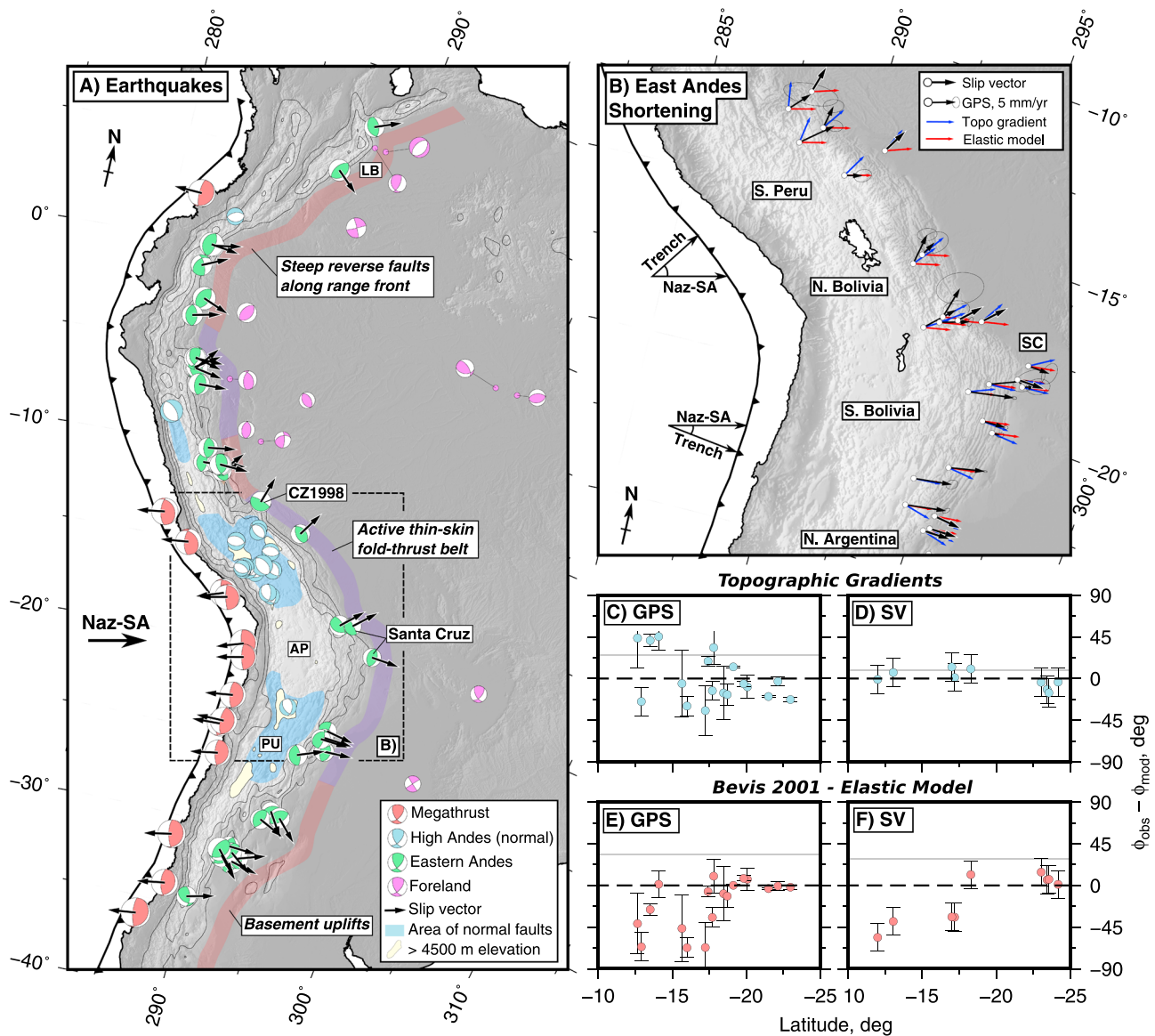
The Eastern Cordillera defines the area between the low-relief, high-elevation Andean plateau, and the sub-Andean lowlands (Figure 1a). Seismicity in this region consists mainly of moderate magnitude reverse and strike-slip faulting, such as the 1998  $M_w$  6.6 Aiquile earthquake (Funning et al., 2005; AQ1998 in Figure 1a). The N-S trending strike-slip rupture of the Aiquile earthquake cuts across preexisting fold-thrust belt structures that were active at  $\sim 10$  Ma, which indicates that the intermediate principal stress has switched from being horizontal at the time in which the fold-thrust belt was active, to vertical (Funning et al., 2005). This transition in stress state can be accounted for by recent uplift of the Eastern Cordillera (Gubbels et al., 1993; Lamb & Hoke, 1997), during which the forces due to contrasts in gravitational potential energy between the Eastern Cordillera and lowlands increased, such that they now balance the compressional forces transmitted across the sub-Andean ranges into the orogen interior.

North of the Aiquile earthquake epicenter are the Cochabamba and Punata basins (Figure 1a). These asymmetrical half grabens are filled with post-Miocene sediments and are bounded by large ( $\sim 2$ -km basement relief), NE-SW to E-W striking normal faults (Renner & Velasco, 2000), which are roughly perpendicular to the trend of the range front in the adjacent sub-Andes. Kennan (1993) proposed that the basins formed predominantly through range-parallel (NW-SE) extension. Faults with a similar geometry relative to the orogen front are seen in southern Tibet (e.g., Armijo et al., 1986) and have been attributed to the influence of potential energy contrasts driving radial spreading of the mountains over the adjacent rigid foreland (e.g., Armijo et al., 1986; Copley, Avouac, & Wernicke, 2011)—a feature reflected in the earthquake slip vectors and GPS data from the Andes discussed in the next section. A similar process may account for the range-perpendicular normal faults at Cochabamba and Punata.

### 3.3. Faulting in the Sub-Andes and Peru-Chile Trench

Faulting on the western edge of the Andes is dominated by large-magnitude ( $M_w > 7.5$ ) megathrust earthquakes along the subduction interface between the Andean forearc and the subducting Nazca plate (e.g., Lin et al., 2013; Pritchard et al., 2007; Sladen et al., 2010). Slip in these megathrust earthquakes is consistently parallel to independent estimates of the orientation of motion between the Nazca plate and the South American shield (DeMets et al., 2010; Norabuena et al., 1999; Figure 9a). Although there is evidence of recent reverse faulting within the Andean forearc (e.g., Benavente et al., 2017; Hall et al., 2012), motion on these faults is small compared to slip on the megathrust.

Unlike slip on the megathrust, the slip vectors of earthquakes on the eastern side of the Andes vary significantly along strike of the mountain belt, with the most conspicuous changes occurring between south Peru and northern Argentina. North of Cuzco a thrust-faulting earthquake in 1998 (Figure 9a; CZ1998) ruptured the shallow detachment beneath the sub-Andes with a NNE-directed slip vector, which is oriented  $\sim 70^\circ$  anticlockwise to the Nazca-South America plate motion. Moving south between southern Peru and northern Bolivia the earthquake slip vectors rotate clockwise from NNE to NE (Figure 9a). Around the Santa Cruz bend the slip vectors rotate rapidly clockwise by a further  $\sim 30$ – $40^\circ$  to point approximately east (Assumpção & Araujo, 1993; Chinn & Isacks, 1983; Devlin et al., 2012; Figure 9a). Finally, within the sub-Andes of southern Bolivia and northern Argentina the slip vectors remain pointing approximately east, which is oriented  $\sim 20$ – $30^\circ$  clockwise relative to Nazca-South America plate motion. The azimuth of the GPS velocity field in the eastern Andes relative to stable South America also rotates clockwise between south Peru and northern



**Figure 9.** Earthquake and GPS data demonstrating the pattern of deformation in the regions bounding the Andes. (a) The selected waveform-modeled earthquakes and well-constrained gCMT events compiled from the literature and this study (see supporting information Tables S1 and S2 for a list of sources). Thin lines are the 1-, 2-, 3-, and 4.5-km elevation contours from the Gaussian-filtered topography (300-km filter width). The light blue region is the area in which evidence for recent extension has been documented in the high Andes (supporting information Figure S17). LB is the Llanos Basin, AP is the Altiplano, PU is the Puna plateau, and SC is Santa Cruz. Both (a) and (b) are in oblique Mercator projection about the Euler pole of the Nazca-South America convergence taken from DeMets et al. (2010); therefore, slip vectors (SVs) parallel to relative plate motion will be horizontal (McKenzie & Parker, 1967). (b) The azimuth of shortening in the eastern Andes inferred from selected GPS sites (Kendrick et al., 2001; Weiss et al., 2016) and earthquake slip vectors, compared with gradients in the filtered topography (300-km Gaussian filter) and the elastic block model of Bevis et al. (2001). GPS velocities in (b) are shown relative to stable South America with  $1\sigma$  uncertainty ellipses. Panels (c) and (d) compare the azimuth of the topographic gradients with the azimuth of the GPS and earthquake slip vectors, respectively. Panels (e) and (f) compare the predicted azimuths for the block model of Bevis et al. (2001) with the GPS and earthquake slip vectors. The grey lines show the root-mean-square misfit (always positive); see also Table 3.

Argentina, mirroring the pattern in the earthquake slip vectors (Kendrick et al., 2001; Lamb, 2000; Weiss et al., 2016; Figure 9b).

Elastic strain accumulation within the Andes from oblique subduction of the Nazca plate beneath the Andean forearc has been proposed to account for the rotation in the GPS velocities in the eastern Andes (Bevis & Martel, 2001; Bevis et al., 2001). Although the elastic model of Bevis et al. (2001) fits the azimuth of GPS velocities south of the Santa Cruz bend, in southern Peru and northern Bolivia it consistently underpredicts the northward component of the GPS velocities and earthquake slip vectors (Figures 9b, 9e, and 9f and see

**Table 3**

*Results of a Statistical Comparison Between the Azimuth of the GPS Velocity Field and Slip Vectors (SVs) in the Eastern Andes, With the Elastic Model of Strain Accumulation on the Peru-Chile Megathrust From Bevis et al. (2001) and the Azimuth of Topographic Gradients (e.g., Copley & McKenzie, 2007)*

Test	RMS, deg	Test 1: All		Test 2: N. of Santa Cruz	
		Megathrust	Topography	Megathrust	Topography
SV	RMS, deg	29	9	42	7
GPS	RMS, deg	33	25	42	31

*Note.* A map view of the measurement sites and their azimuths is shown in Figure 9b. Topographic gradients were calculated from a 300-km Gaussian-filtered version of the SRTM 3-arc sec elevation model (Farr et al., 2007). Filter widths between 100 and 400 km give similar results. RMS is the root-mean-square misfit between the observed and modeled azimuth. Two tests are shown, one in which all GPS and slip vector measurements shown in Figure 9b are used to compute the misfits (Test 1), and one in which only measurements from north of Santa Cruz are used to compute the misfits (Test 2). In all cases the azimuth of the topographic gradients fit the observations better than the model of elastic strain accumulation of Bevis et al. (2001). SRTM = Shuttle Radar Topography Mission; RMS = root-mean-square.

Table 3). These spatially coherent misfits imply the elastic models are not accurately capturing the orientation of the shortening direction in the sub-Andes. In addition, the assumption in Bevis et al. (2001) that shortening in the sub-Andes can be modeled as slip parallel to Nazca-South America plate motion on a detachment horizon beneath the sub-Andes is not consistent with the observed earthquake slip vectors (Figure 9a).

Alternatively, if the eastern Andes are deforming predominantly in response to horizontal contrasts in gravitational potential energy, then the direction of shortening will be parallel to topographic gradients (e.g., Copley & McKenzie, 2007; Flesch & Kreemer, 2010; Lamb, 2000). We find that earthquake slip vectors in the sub-Andes are consistently parallel to gradients in the topography (Figures 9b and 9d and Table 3). The topographic gradients also match the general pattern of clockwise rotating GPS azimuths between southern Peru and northern Argentina, the northward component of the GPS velocity field near Cuzco, and the rotation of the GPS velocities around the Santa Cruz bend (Figure 9b). In addition, the azimuth of shortening inferred from the GPS and earthquake slip vectors are statistically better fit by the direction of topographic gradients than an elastic model of strain accumulation on the Peru-Chile subduction zone (see statistical comparison in Table 3).

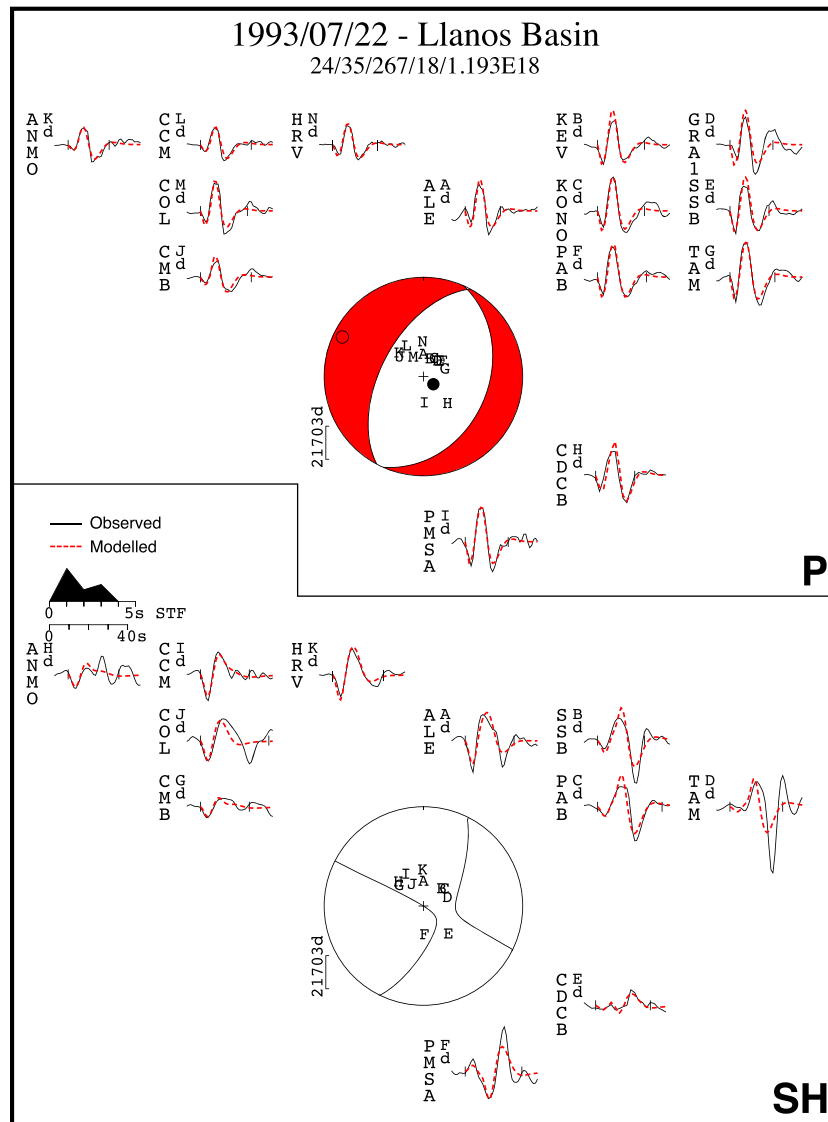
We therefore conclude that the forces resulting from relative plate motion control the orientation of slip on the subduction interface on the western side of the Andes, while contrasts in gravitational potential energy between the mountains and forelands control the orientation of slip on faults in the sub-Andean belt in the east (e.g., Assumpção & Araujo, 1993; Lamb, 2000).

### 3.4. Faulting and Flexure in the South American Forelands

Reverse-faulting earthquakes in regions >300 km from the Andes range front (Figure 9a) indicate the South American foreland crust is breaking in response to compressional forces acting through the lithosphere (Assumpção, 1992). However, within 300 km of the Andes range front, asymmetrical sedimentary basins (McGroder et al., 2015), long-wavelength, negative free-air gravity anomalies (Lyon-Caen et al., 1985), and shallow extensional faulting overlying compressional faulting at the base of the crust (Figures 10, 11a, and 11c) imply that the forelands are bending in response to the load of the Andes (e.g., Lyon-Caen et al., 1985; Watts et al., 1995).

Evidence for extension in the Andes foreland is limited to a single  $M_w$  6.4 normal-faulting earthquake beneath the Llanos Basin (Figure 9a and Table 2). Long-period waveform modeling suggests this earthquake had a centroid depth of  $18_{-5}^{+5}$  km (Figure 10). The Moho beneath the Llanos Basin is at  $\sim$ 40- to 45-km depth (Assumpção et al., 2013), which implies that the normal-faulting earthquake reflects extension in the shallow basement of the bending Andean foreland.

A  $M_w$  5.3 reverse-faulting earthquake has also been recorded beneath the Llanos Basin (Figures 11a and 11c and Table 2). We determined the centroid depth of this earthquake by comparing synthetic waveforms to stacked vertical component seismograms recorded at a small-aperture array in Spitsbergen using the method of Craig et al. (2012). The observed seismograms can be matched by a reverse-faulting earthquake at a



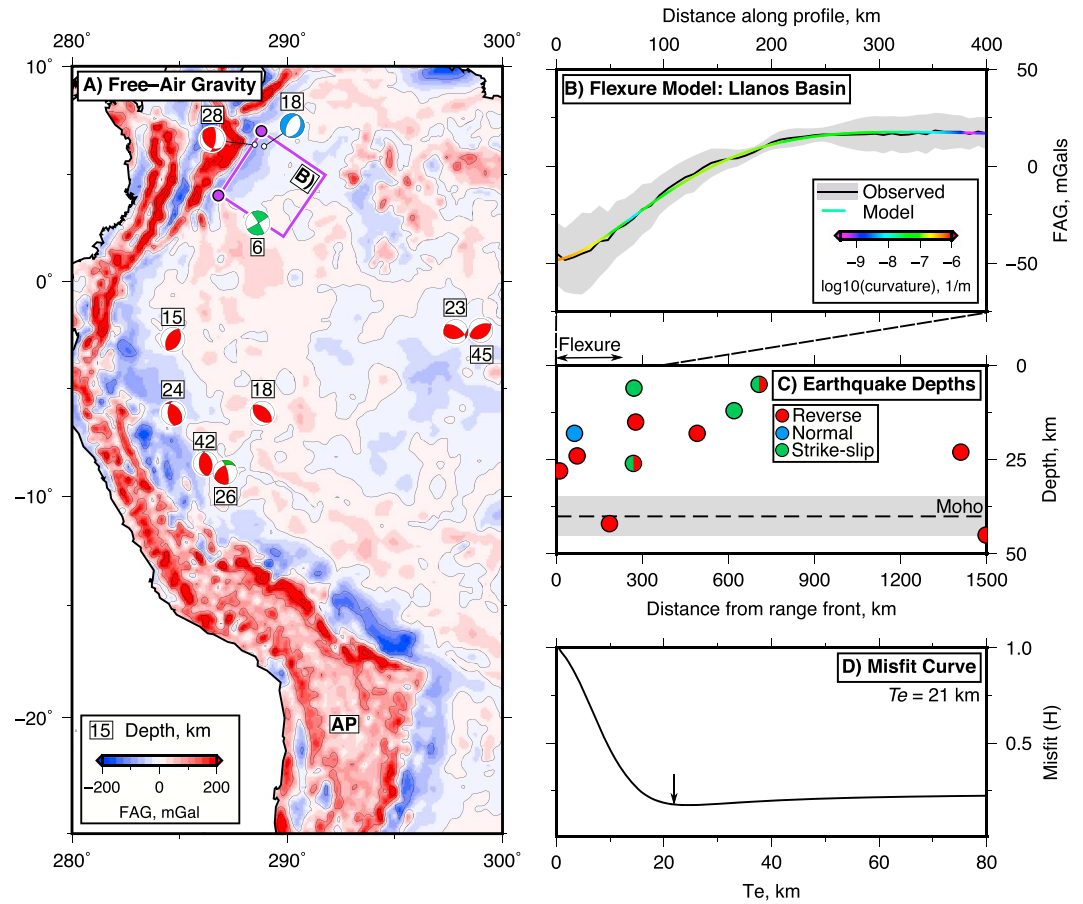
**Figure 10.** Minimum-misfit teleseismic body-waveform solution for the 22 July 1993 Llanos Basin earthquake. Figure layout is the same as for Figure 3. The uncertainties in the fault parameters were estimated using the method described in section 2.2 and are strike =  $\pm 25^\circ$ , dip =  $\pm 5^\circ$ , rake =  $\pm 25^\circ$ , and depth  $\pm 5$  km.

centroid depth of  $28^{+2}_{-2}$  km (supporting information Figure S12). Reverse faulting has also been recorded at 42-km depth beneath the Madre de Dios Basin in central Peru (Assumpção, 1992; Figure 11a), indicating that the bending portion of the South American lithosphere probably remains in compression from 26 to 30 km to at least the base of the crust (Figure 11c).

Observations of shallow extensional earthquakes overlying deeper compressional earthquakes within the continental lithosphere are rare and have only been documented previously in the forelands of Tibet (Maggi, Jackson, Priestley, & Baker, 2000; Molnar et al., 1977; Ni & Barazangi, 1984), and possibly in small ( $M_w < 4.5$ ) earthquakes recorded in the forelands of the Alborz mountains (Nemati et al., 2013). The pattern of earthquakes in both the Tibetan and Andean forelands implies that flexural stresses are large enough to break faults in underthrusting continental lithosphere.

If we treat the flexed South American forelands as a thin bending plate, the magnitude of the flexural stresses can be related to the curvature of the plate, and a factor that is governed by the assumed rheology of the plate (Turcotte & Schubert, 2002):





**Figure 11.** Free-air gravity data, earthquakes, and plate models used to study the flexure of the South American forelands. (a) The EIGEN-6c free-air gravity map of South America (Shako et al., 2014) low pass filtered to exclude signals with wavelength  $<50$  km that are unrelated to flexure (e.g., Bry & White, 2007). The purple box is the region within which profiles through the gravity field perpendicular to the Andes range front have been extracted and stacked. AP marks the Altiplano. (b) shows the stacked free-air gravity anomalies with 1 standard deviation ( $\sigma$ ) bounds, and the best fit model to the observed gravity profile of an elastic plate overlying an inviscid half-space bending in response to a line load and bending moment (e.g., Turcotte & Schubert, 2002). We assume that the sediments in the foreland basin are  $500 \text{ kg/m}^3$  less dense than the mantle beneath the plate, and Young's modulus and Poisson's ratio of the plate are  $10^{11} \text{ Pa}$  and 0.25, respectively (Turcotte & Schubert, 2002). The color of the line shows the absolute curvature of the plate model. (c) The mechanisms of waveform-modeled foreland earthquakes as a function of distance from the Andes range front. The Moho depth and uncertainty ( $1\sigma$ ) is taken from the catalogue of Assumpção et al. (2013). (d) The weighted misfit between the model and observations computed for a range of elastic thicknesses, defined as  $H = \frac{1}{N} \sum \left[ \frac{g_m - g_o}{\sigma} \right]^2$ , where  $g_m$  and  $g_o$  are the modeled and observed free-air gravity, respectively, and  $N$  is the number of measurements along the profile.

$$\sigma_f = \frac{ET}{2(1-\nu^2)} \frac{d^2w}{dx^2}, \quad (1)$$

where  $\sigma_f$  is the maximum flexural stress,  $E$  is Young's modulus,  $\nu$  is Poisson's ratio,  $T$  is either the effective elastic thickness of the plate (in a purely elastic model), or the thickness of the aseismic elastic core (in an elastic-plastic model with a constant yield stress), and  $\frac{d^2w}{dx^2}$  is the curvature of the plate.

To estimate the curvature and effective elastic thickness ( $T_e$ ) of the South American foreland beneath the Llanos Basin, we followed the method of McKenzie and Fairhead (1997) and modeled the free-air gravity anomalies produced by flexure of an elastic plate overlying an inviscid mantle half-space, with the plate overlain by low-density sediments. We find the gravity anomalies in the Llanos Basin can be fit by a plate model with a  $T_e$  of at least 20 km (Figures 11b and 11d). However, the misfit between the modeled and observed gravity field at large  $T_e$  values increases by only a fraction of the minimum misfit, suggesting that our

estimate represents only a lower bound (Figure 11d). Our results are consistent with those of Pérez-Gussinyé et al. (2007) and McKenzie et al. (2014), who find that  $T_e$  in the Andean forelands is between 15 and 25 km, which is significantly smaller than the seismogenic thickness (40–45 km; Assumpção & Suarez, 1988; Emmerson, 2007). Stewart and Watts (1997) found a larger  $T_e$  of 50 km in the Llanos Basin; however, their study relied on modeling individual Bouguer gravity profiles and fixed the location of the plate break, which has typically been shown to overestimate  $T_e$  (see discussion in Jackson et al., 2008).

The maximum curvature of the plate in the best fit model is  $\sim 4 \times 10^{-7} \text{ m}^{-1}$  (Figure 11b). Assuming the plate has a Young's modulus of  $10^{11} \text{ Pa}$  and Poisson's ratio of 0.25, equation (1) would give a maximum extensional flexural stress of  $\sim 530 \text{ MPa}$ . This stress will subject normal faults in the top half of the bending plate, which dip at  $\sim 35^\circ$  relative to the plate surface (e.g., Llanos Basin earthquake; Figure 10), to average shear stresses  $\lesssim 130 \text{ MPa}$ . For a simple elastic-plastic plate with a constant yield stress (Turcotte & Schubert, 2002), and an elastic core  $< 17 \text{ km}$  thick (based on the depth distribution of earthquakes; Figure 11c), the maximum flexural stresses are reduced to  $\lesssim 360 \text{ MPa}$ , and the average shear stresses on faults to  $\lesssim 90 \text{ MPa}$ . Further, earthquakes could reduce our estimate of the elastic core thickness and therefore reduce our stress estimates.

In contrast to the bending portion of the South American forelands, the normal faulting in the high Andes and reverse faulting throughout the foreland crust  $> 300 \text{ km}$  from the Andes range front appears to be primarily controlled by the forces per unit length exerted between the mountains and South America due to lateral contrasts in gravitational potential energy. In the next section we present calculations to estimate the forces acting through the South American forelands and place an upper bound on the frictional strength of faults within the foreland crust.

## 4. Strength of the South American Forelands

### 4.1. Forces Acting Between the Andes and the South American Forelands

The forces per unit length due to potential energy contrasts between a mountain belt and its adjacent foreland can be calculated from lateral contrasts in the density structure between the two regions (e.g., Artyushkov, 1973; Dalmayrac & Molnar, 1981). We build on the original calculations of Dalmayrac and Molnar (1981) by using new estimates of the temperature structure, chemical composition, and thickness of the crust and mantle lithosphere to refine the estimates of the forces per unit length acting between the Andes and South America, following a method similar to that of Copley and Woodcock (2016). A summary of the parameters used in the calculations is provided in Table 4; the choice of parameters and the methodology behind the calculations are described in detail in the supporting information, and an overview of the calculations is provided below.

We compute the horizontal force per unit length exerted between the Andes and South America by integrating the differences in vertical normal stress between the mountains and forelands ( $\Delta\sigma_{zz}$ ) from the surface to the depth of isostatic compensation ( $F_{GPE} = \int \Delta\sigma_{zz} dz$ ; Dalmayrac & Molnar, 1981). By varying the temperature structure, composition, and thickness of the crust and mantle lithosphere, we find that the horizontal force per unit length acting between the Andes and the South American foreland is  $\sim 4\text{--}8 \times 10^{12} \text{ N/m}$  along strike of the mountain range (Figure 12a). This result is consistent with previous studies (Dalmayrac & Molnar, 1981; Froidevaux & Isacks, 1984; Husson & Ricard, 2004; Meijer et al., 1997; Molnar & Lyon-Caen, 1988; Oncken et al., 2012) but includes a larger range of uncertainty that is related to the range in possible lithospheric mantle thickness and the poorly constrained temperature structure beneath the Andes that had previously not been considered (e.g., Molnar & Stock, 2009; see supporting information).

### 4.2. Fault Friction in the South American Forelands

The forces per unit length due to contrasts in gravitational potential energy acting between the Andes and South America must be balanced by the forces acting through the South American foreland lithosphere. Reverse-faulting earthquakes throughout the nonbending regions of the South American forelands, outboard of the region of normal faulting in the high Andes, implies that these forces are large enough to exceed the static frictional strength of faults in the forelands (as is also seen in the Tibetan foreland in India; Copley, Avouac, Hollingsworth, & Leprince, 2011).

We construct one-dimensional yield stress profiles that reflect the stress state as a function of depth to the east of the sub-Andean belt in the bending and nonbending part of the South American foreland and integrate the yield stress to estimate the force the lithosphere can support in these different regions ( $F_{fl} = \int \Delta\sigma_{xx} dz$ ; e.g., Brace & Kohlstedt, 1980; Goetze & Evans, 1979). We then compare these estimates of foreland strength

**Table 4**

*Parameters Used in the Calculations for the Force Exerted Between the Mountain Range and Forelands, and for Estimating the Frictional Strength of Faults in the South American Forelands*

Variable	Value	Source
Crustal thickness, lowlands	35–45 km	Assumpção et al. (2013)
Crustal thickness, Andes	65–80 km	Assumpção et al. (2013)
Lithosphere thickness, lowlands	120–140 km	McKenzie and Priestley (2008)
Lithosphere thickness, Andes	180–220 or 0 km	See supporting information
Moho temperature, lowlands	600–700 °C	See supporting information
Moho temperature, Andes	700–1,000 °C	Weber et al. (2002)
Mantle potential temperature	1,315 °C	McKenzie et al. (2005)
Thermal expansivity <sup>a</sup> , crust	$3 \times 10^{-5} \text{ K}^{-1}$	Turcotte and Schubert (2002)
Thermal expansivity <sup>a</sup> , mantle	$3-4.5 \times 10^{-5} \text{ K}^{-1}$	Bouhifd et al. (1996)
Asthenosphere density ( $\rho_a$ , 0 °C)	3,330 kg/m <sup>3</sup>	Turcotte and Schubert (2002)
Lithospheric Mantle density (0 °C)	$\rho_a - 50 \text{ kg/m}^3$	Lucassen et al. (2005) and McKenzie and Priestley (2016)
Crustal density (0 °C)	2,800 kg/m <sup>3</sup>	Lucassen et al. (1999)
Foreland fault dips	30–50°	This study
Activation energy ( $E$ )	540 kJ/mol	Karato and Wu (1993)
Activation volume ( $V$ )	20 cm <sup>3</sup> /mol	Karato and Wu (1993)
Stress exponent ( $n$ )	3	Karato and Wu (1993)
Seismogenic thickness	40–45 km	Assumpção and Suarez (1988)
Foreland sediment thickness	5–8 km	McGroder et al. (2015)
Neutral fiber depth	13–28 km	See section 3.4
Elastic core thickness <sup>b</sup>	1–20 km	See caption

<sup>a</sup>This is the linear coefficient of thermal expansion. <sup>b</sup>The elastic core thickness is the extent of the region either side of the neutral fiber in the bending South American foreland over which the stress field changes from being extensional to compressional.

( $F_f$ ) with our estimate of the forces per unit length acting through the foreland lithosphere ( $F_{GPE}$ ) to place an upper bound on the frictional strength of faults in the South American crust.

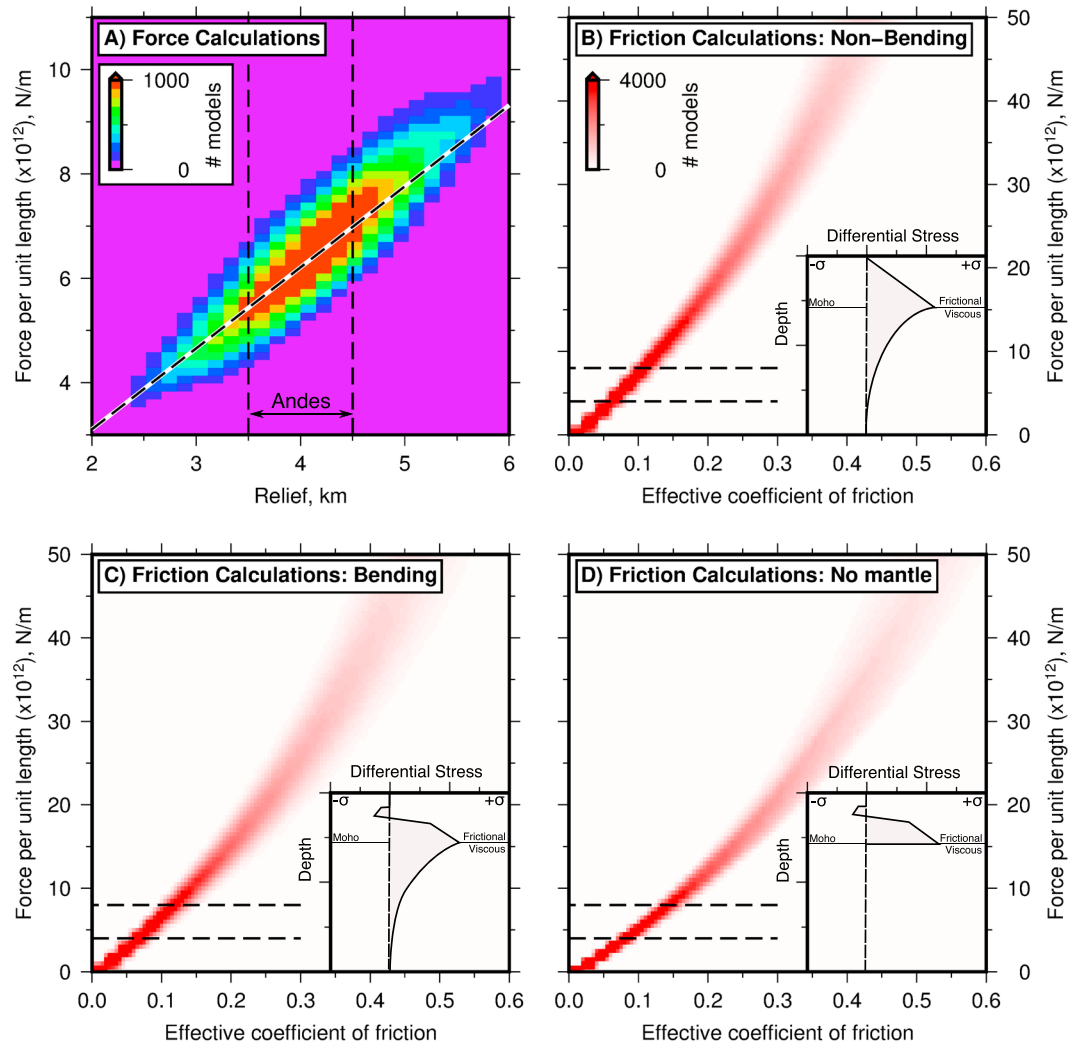
Faults modulate the strength of the brittle portion of the lithosphere, which can be expressed as a function of the effective coefficient of friction (Turcotte & Schubert, 2002):

$$\Delta\sigma_{xx} = \frac{2\mu' \rho g z}{\pm \sin 2\theta - \mu'(1 + \cos 2\theta)}, \quad (2)$$

where  $\mu'$  is the effective coefficient of friction,  $\rho$  is the average crustal density,  $g$  is the acceleration due to gravity,  $z$  is the depth,  $\theta$  is the angle of the fault from the vertical, and  $\Delta\sigma_{xx}$  is the horizontal differential stress the faults can support. The  $\pm \sin 2\theta$  term is negative if the faults are extensional and positive if they are compressional.

Within 300 km of the Andes range front the top ~5–8 km of the crust consists of sedimentary basins that contain no earthquakes (McGroder et al., 2015; Figure 11c) and that we assume support negligible force. Outside of the sedimentary basins, earthquakes occur throughout the thickness of the crust (Assumpção, 1992; Assumpção & Suarez, 1988; this study; Figure 11c), and therefore, we assume that stresses in the basement crust are supported by frictional resistance on faults given by equation (2).

Earthquakes are absent from the foreland mantle lithosphere beneath South America (Figure 11c). A similar pattern of seismicity has been observed in other continental shield regions (e.g., India (Craig et al., 2012; Maggi, Jackson, McKenzie, & Priestley, 2000); Africa (Craig et al., 2011); Siberia (Sloan et al., 2011)) and has been attributed to the temperature of the continental lithospheric mantle generally exceeding ~600 °C (Jackson et al., 2008; McKenzie et al., 2005), above which mantle rocks deform predominantly by ductile creep



**Figure 12.** Results of calculations for the forces per unit length acting through the South American lithosphere, due to differences in gravitational potential energy between the Andes and the South American forelands. (a) The force calculations as a function of relief between the mountains and forelands (described in section 4.1). Vertical black dashed lines delineate the range of appropriate solutions for the Andes. The dashed black and white line defines the relationship between relief and force assuming crustal isostasy, with a crustal thickness of 70 and 40 km in the mountains and lowlands, respectively. (b–d) The results of calculations for the maximum force that can be supported by the foreland lithosphere as a function of the effective coefficient of friction along faults, as described in the section 4.2. The three different cases shown are (b) when the whole crust is in compression and there is no sediment layer (i.e., the foreland outside the bending region); (c) when the top 5–8 km of crust is sediment that supports no force, the top 5–13 km of basement is in extension, and the bottom ~20 km is in compression (i.e., the foreland in the bending region); and (d) the end-member scenario when the lithosphere is bending, and the mantle supports no stress at all. Schematic yield stress profiles are shown inset. Horizontal black dashed lines are the bounds on the horizontal force acting through the South American lithosphere from the calculations in (a). Where the envelope of models plots above these horizontal dashed lines, the lithosphere would be too strong to break in earthquakes in response to the forces generated by contrasts in gravitational potential energy acting between the mountains and forelands.

mechanisms. We use a dry olivine dislocation creep law to estimate an upper bound on the ductile strength of the lithospheric mantle (Karato & Wu, 1993):

$$\Delta\sigma_{xx} = S\dot{\epsilon}_r^{\frac{1}{n}}A^{-\frac{1}{n}}\exp\left(\frac{E+pV}{nRT}\right), \quad (3)$$

where  $S$  is the shear modulus,  $\dot{\epsilon}_r$  is the reference strain rate which we calculate by imposing stress continuity at the brittle-ductile transition,  $A$  is a constant,  $n$  is the power law exponent,  $E$  is the active energy,  $p$  is the

pressure,  $V$  is the activation volume,  $R$  is the gas constant, and  $T$  is the temperature (parameters given in Table 4). It has been suggested that upper mantle rocks at temperatures less than 750 °C may deform by low temperature plasticity (Peierl's creep; e.g., England & Molnar, 2015; Mei et al., 2010), which would support smaller differential stresses for a given strain rate than dislocation creep. If so, the forces supported by faults in the lithosphere would be slightly higher than our estimates. However, we also perform calculations in which the lithospheric mantle supports no stress, providing an absolute upper bound on the possible forces acting on faults within the crust.

By performing a parameter sweep through the range of variables that control the shape of the yield stress envelope with depth (effective coefficient of friction, seismogenic thickness, fault dips, neutral fiber depth, elastic core thickness, and sediment thickness; parameter range given in Table 4), we can define an envelope of the force that the lithosphere can support as a function of the effective coefficient of friction on crustal faults (Figures 12b–12d). We find that, in order to break in response to the  $4\text{--}8 \times 10^{12}$  N/m that we estimate above to be acting through the forelands, faults in the bending and nonbending regions of South America must have an effective coefficient of friction  $\lesssim 0.15$ . If the lithospheric mantle supported no stress at all, which would resolve all the force acting through the foreland lithosphere onto faults in the crust, the maximum possible effective coefficient of friction would be 0.2 (Figure 12d). If the faults in the South American crust were stronger, then they would not be breaking in earthquakes as a result of the forces per unit length generated by gravitational potential energy contrasts between the Andes and its bounding lowlands.

Our low estimate of the effective coefficient of friction on faults in the South American crust is consistent with studies that infer elevated pore fluid pressures (Sibson, 2004) or foliated, phyllosilicate-rich fault gouges (Collettini et al., 2009; Imber et al., 2008) may reduce the frictional strength of active fault zones relative to laboratory estimates of bare rock friction (Byerlee, 1978). Notably, faults in the forelands with an effective coefficient of friction  $\lesssim 0.2$ , that dip between 30° and 50° (Figure 10), will support depth-averaged shear stresses  $\lesssim 110$  MPa, which is similar to our estimate derived from the analysis of flexure in section 3.4.

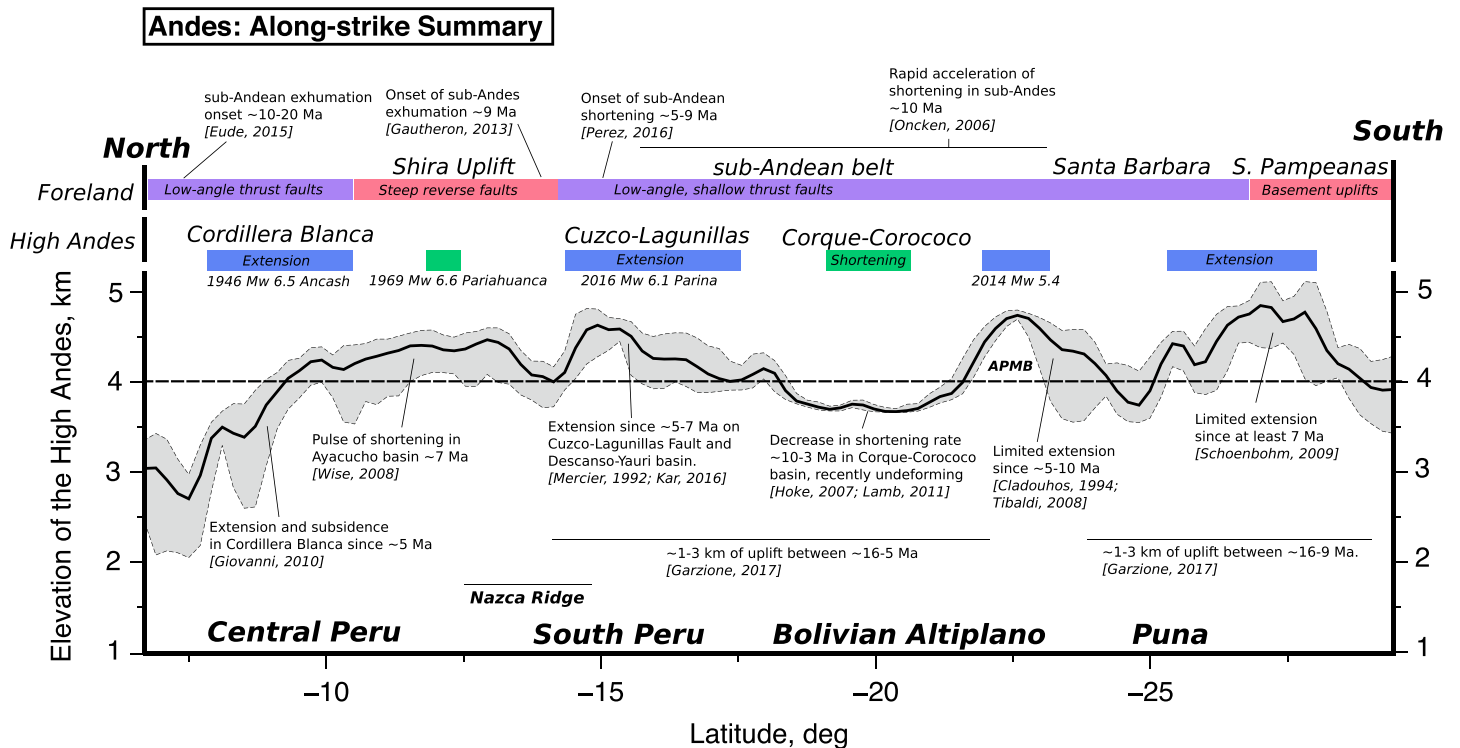
Previous studies of the dynamics in South America based on a thin-viscous sheet approximation (England & McKenzie, 1982) imply the deviatoric stresses acting to deform the lithosphere are relatively small ( $\sigma'_{xx} \approx 10\text{--}30$  MPa; Dalmayrac & Molnar, 1981; Flesch & Kreemer, 2010; Lamb, 2000). Our estimates of the horizontal forces acting through the  $\sim 100\text{--}150$ -km-thick foreland lithosphere imply deviatoric stresses on the order of a few tens of megapascals, which is consistent with the aforementioned studies.

## 5. Discussion

### 5.1. Late Miocene Change in the Dynamics of the Andes

The Parina earthquake and the surrounding seismicity demonstrates that the high Andes in south Peru are currently undergoing extension. A  $M_w$  6.2–6.8 normal-faulting earthquake recorded in 1946 at Ancash in central Peru (Doser, 1987; Heim, 1946), and a  $M_w$  5.4 earthquake in the Bolivian Altiplano (Figure 9a), suggests that a wider region of the high central Andes is also currently extending.

Geological evidence of recent normal faulting in the high Andes is widespread, with examples of extensional structures in regions at elevations  $>3,000$  m from central and southern Peru (Benavente et al., 2013; Dalmayrac & Molnar, 1981; Kar et al., 2016; Mercier et al., 1992; Sébrier et al., 1985, 1988; Veloza et al., 2012), northern Chile (Tibaldi & Bonali, 2018; Tibaldi et al., 2009), southern and northern Bolivia (Lamb, 2000; Lavenu et al., 2000; Mercier, 1981), and northern Argentina (Cladouhos et al., 1994; Lavenu et al., 2000; Marrett et al., 1994; Schoenbohm & Strecker, 2009; Figures 9a and 13). The timing of motion on these normal faults can be bracketed by cross-cutting relationships with the extensive volcanics erupted continually throughout the Andean orogeny. The earliest evidence of extension in the high Andes varies from  $\sim 7\text{--}9$  Ma in southern Bolivia and northern Argentina (Cladouhos et al., 1994; Montero Lopez et al., 2010) to  $\sim 5\text{--}7$  Ma in central and southern Peru (Benavente et al., 2013; Cabrera et al., 1991; Giovanni et al., 2010; Kar et al., 2016; Mercier, 1981) and follows an earlier period of widespread approximately E-W compression (Elger et al., 2005; Ellison et al., 1989; Megard et al., 1984; Mercier et al., 1992; Sébrier et al., 1985; Tibaldi et al., 2009). Within the central Bolivian Altiplano folded Pliocene strata in the Corque–Corococo basin imply the shallow crust experienced waning shortening between  $\sim 10$  and 3 Ma (Hoke & Lamb, 2007; Lamb, 2011) and has recently been undeforming (Elger et al., 2005; Lamb, 2011; Figure 13). The transition in stress state within parts of the high Andes of Peru and Argentina from dominantly compression to extension since the late Miocene, and the slowing



**Figure 13.** Summary of the topography and recent deformation history in the Andes between central Peru and northern Argentina. Topography is extracted in a 30 km swath down the spine of the range from a 100-km Gaussian-filtered version of the SRTM 3-arc sec elevation model. The maximum, mean, and minimum elevations are shown. Evidence for the timing and pattern of deformation in the high Andes and the adjacent foreland is summarized above and below the elevation curve. APMB is the Altiplano-Puna magma body.

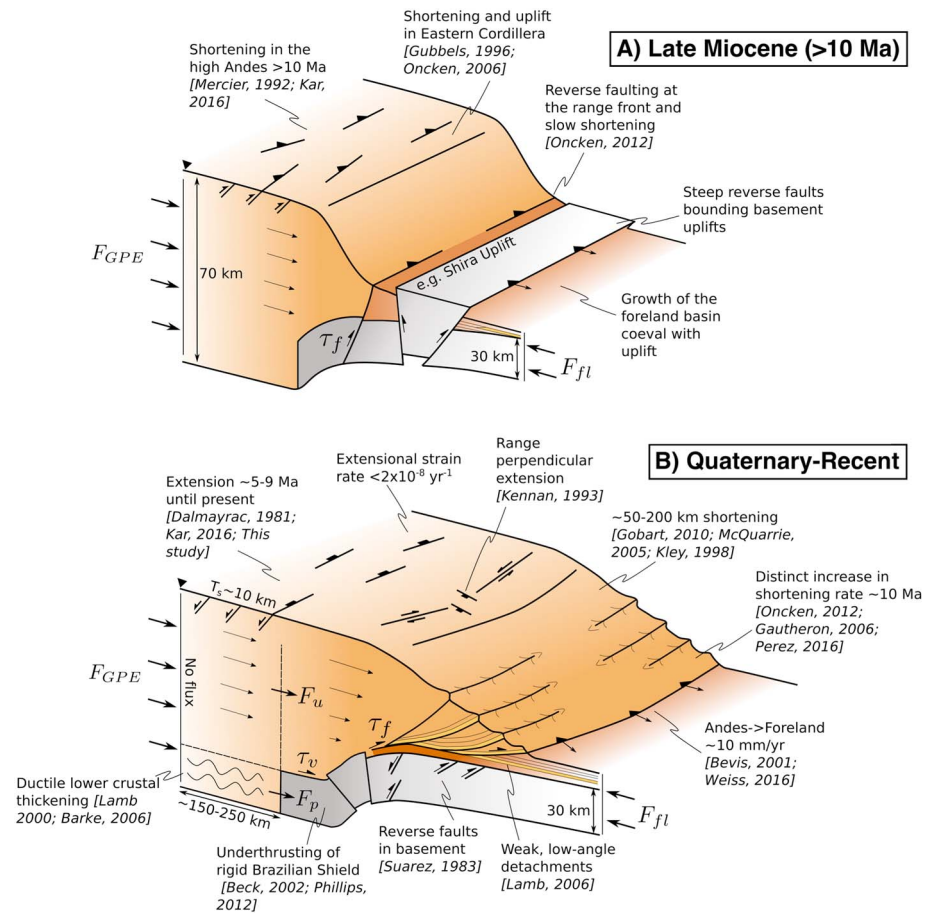
of shortening in the lower elevation Bolivian Altiplano, is indicative of an orogen-wide change in the force balance.

Over the same time interval (~5–16 Ma) paleoelevation proxies infer there has been 1–3 km of surface uplift in the high Andes of southern Peru and Bolivia (e.g., Barke & Lamb, 2006; Garzzone et al., 2006, 2008, 2017; Kar et al., 2016; Saylor & Horton, 2014). In addition, structural reconstructions and proxies for rock exhumation have recorded a distinct shift in the locus, rate, and style of deformation on the eastern edge of the Andes. Prior to ~10-Ma deformation in the eastern Andes consisted of slow, long-wavelength folding and bivergent reverse faulting of lower Paleozoic strata and metamorphic basement focused in the Eastern Cordillera (Espurt et al., 2008; Kley, 1996; Oncken et al., 2006; Perez et al., 2016). Since ~10 Ma, shortening rates in the eastern Andes have increased significantly (Oncken et al., 2006, 2012), and the locus of deformation has propagated rapidly eastward into the sub-Andean lowlands (Echavarría et al., 2003; Gautheron et al., 2013; Gubbels et al., 1993; Perez et al., 2016), where Mesozoic foreland basin fill is exposed in short-wavelength (~5–10 km) anticlinal ridges bound by closely spaced splay faults above shallow-dipping detachments (e.g. Kley, 1996).

Any attempt to explain the onset of normal faulting in the high Andes ~5–9 Ma must also account for the observations described above (summarized in Figure 13).

### 5.2. Possible Causes of Normal Faulting in the High Andes

Removal of dense lower crust and mantle lithosphere (delamination) could increase the gravitational potential energy contrast between the mountains and forelands, leading to extension in the highest parts of the Andes (e.g., England & Houseman, 1989; Garzzone et al., 2006). Delamination has been proposed to account for the composition, timing, and volume of ignimbrite and mafic volcanism (e.g., Kay & Mahlburg Kay, 1993), the Helium isotope ratios of hydrothermal fluids (Hoke & Lamb, 2007), and the possible rapid Miocene-recent uplift of the central Andes (e.g., Garzzone et al., 2006, 2008, 2017). However, the relationship between crustal thickening and uplift rates in the Bolivian Altiplano (Lamb, 2011, 2016), and inconsistent seismic models that independently infer thick, thin, and variable thickness lithospheric mantle beneath the Andes (e.g., Beck &



**Figure 14.** Sketch of the evolution of faulting in the Andes since the late Miocene. A reduction in the frictional shear stresses ( $\tau_f$ ) along the base of the eastern Andes ~5–9 Ma would have reduced the horizontal force acting through upper crust overriding the rigid foreland ( $F_u$ ). A reduction in  $\tau_f$  would be balanced ( $F_{GPE} = F_u + F_p$ ) by an increase in the viscous resistance to shortening in the ductile lower crust ( $F_p$ ), extensional viscous strain within the center of the mountain belt, and an increase in the rate of propagation of the mountains over the rigid foreland.

Zandt, 2002; Phillips et al., 2012; Priestley & McKenzie, 2013; Ward et al., 2016; Whitman et al., 1992), calls into question whether delamination beneath the central Andes coeval with extension actually occurred.

Another mechanism that has been suggested to induce extension in the high Andes is dynamic uplift of central Peru due to the subduction of the buoyant Nazca Ridge (Margirier et al., 2017; McNulty & Farber, 2002; Mercier et al., 1992). Our observations of normal-faulting earthquakes 400 km south of the Nazca Ridge (Figure 13), in addition to evidence of extensional faulting within elevated regions across the Andes, irrespective of the nature of the underlying subducting plate (e.g., flat slab segments; Gutscher et al. (2000)), indicate that the pattern of extension is probably unrelated to subduction processes. Similarly, the timing and distribution of normal-faulting earthquakes appear unrelated to the subduction zone earthquake cycle.

Changes in the horizontal forces supported by the lithosphere bounding the Andes could also cause the onset of extension in the high mountains. The switch in shortening style in the eastern Andes ~10 Ma from steeply dipping reverse faulting to shallow-dipping, weak detachment faulting within the foreland basin sediments could have reduced the shear stresses acting on the base of the overriding Andean lithosphere, leading to the onset of extension in the high mountains, a reduction in shortening rates in the Bolivia Altiplano, and enhanced shortening rates within the lowlands of the eastern Andes (Babeyko et al., 2006; Oncken et al., 2012). We explore this possibility further below.

The spatial relationship between normal faulting and foreland deformation style is suggestive of a causal link. Late Miocene to recent normal faulting in the high Andes correlates along strike with regions of wide thin-skinned fold-thrust belts (Kley et al., 1999), the locations of low-angle thrust-faulting earthquakes (Devlin

et al., 2012), and thick Paleozoic and Mesozoic sediments in the adjacent foreland basin (McGroder et al., 2015; supporting information Figure S17). In contrast, in regions where the active foreland deformation style comprises predominantly reverse faulting emerging at the front of steep topography (e.g., Shira Uplift of Peru, Kley et al., 1999; Sierra Pampeanas of Argentina, Alvarado & Beck, 2006; Oriente of Ecuador, Kley et al., 1999) the style of faulting in the adjacent high Andes is dominantly compressional (Figure 13). A particularly clear example is seen in the high Andes adjacent the Shira Uplift in Peru, where faulting in the 1969  $M_w$  6.1 and 6.6 Pariahuanca earthquakes was compressional (Philip & Megard, 1977; Sébrier et al., 1988; Suarez et al., 1983; see PH1969; Figure 1a). However, both north and south of Shira, where the foreland has wide and active thin-skinned fold-thrust belts (Kley et al., 1999), the high Andes are undergoing extension (Devlin et al., 2012; Doser, 1987; Heim, 1946; this study; Figures 1a and 13).

It is possible that once the Andes reached the maximum elevation that could be supported by the steep reverse faults bounding the eastern edge of the range  $\sim 5$ – $9$  Ma (Figure 14a), the plateau widened as faulting propagated eastward into the thick foreland basin sediments that had accumulated concomitant with uplift (e.g., Molnar & Lyon-Caen, 1989). Foreland deformation then became focused along weak detachment layers above the sediment-basement interface, and the rigid Brazilian Shield was underthrust further beneath the mountains (Kley et al., 1999; Lamb, 2006, 2011; Phillips et al., 2012; Figure 14b). As the force balance in the eastern Andes is controlled by the horizontal shear stresses acting on the base of the overriding lithosphere (e.g., Huppert, 1982; McKenzie et al., 2000), reducing the frictional shear stresses along the nose of the foreland fold-thrust belt would be balanced by extensional viscous strain and normal-faulting within the overriding lithosphere (see the calculations presented in Craig & Copley, 2018). In addition to the onset of extension within the high Andes, the ductile lower crust in front of the indenting foreland lithosphere would shorten and thicken (Barke & Lamb, 2006; Lamb, 2011), balancing the flux of material out over the South American foreland. At the surface this would be visible as the mountains spreading eastward over the forelands coeval with extension in the highest parts of the range—a feature that is reflected in the current pattern of crustal deformation (Figure 14b).

Previous models of the dynamics in the Andes have typically treated the mountain belt in terms of vertically averaged stress and strain (i.e., a thin-viscous sheet; Flesch & Kreemer, 2010; Lamb, 2000; Liu et al., 2002). Under the thin-sheet assumptions shear stresses on the base of the lithosphere are negligible, and weakening the eastern side of the Andes would simply enhance shortening strain rates in that region to maintain the horizontal force balance. Our insight is to include the influence of the underthrust South American foreland, which will partition the force balance with depth beneath the mountains (i.e.,  $F_u$  and  $F_p$  in Figure 14b), and accommodate extension of the upper crust in the Andes.

### 5.3. Implications for the Evolution of Orogenic Belts

A generalization of the model presented above, in which mountain belts weaken their forelands through synorogenic sedimentation, is likely to be broadly applicable to orogen evolution (e.g., Copley et al., 2009; Lamb, 2006; Reynolds et al., 2015). For example, the deformation style within the forelands of the Tien Shan is dependent on the thickness of the sedimentary basins bounding the basement uplifts (Kober et al., 2013). Along range fronts adjacent to thick (10–15 km) sedimentary basins, anticlinal folding above buried reverse faults extends  $\sim 30$  km into the piedmont, suggesting shortening is beginning to step out from the basement-cutting faults onto low-angle detachments in the foreland stratigraphy (Avouac & Tapponnier, 1993). However, in regions where the basin sediments are thin ( $< 5$  km), faulting has remained focused along steep reverse faults that outcrop at the range front (Avouac & Tapponnier, 1993). Quaternary-Holocene fault scarps (Thompson et al., 2002), and recent seismicity (Sloan et al., 2011), indicate shortening is still active throughout the interior of the Tien Shan, which probably reflects the fact that the steep, basement-cutting reverse faults can still transmit enough force into the mountain range to overcome the gravitational body forces acting to drive extension.

In contrast, within the southern forelands of Tibet, deformation has focused onto detachment horizons that cut through the foreland stratigraphy, and emerge  $\sim 80$ – $100$  km south of the high Himalaya (Lavé & Avouac, 2000). Geomorphic evidence for uplift (Lavé & Avouac, 2000), and the pattern of shortening reflected in thrust-faulting earthquakes (Molnar & Lyon-Caen, 1989), is confined to the edges of the mountain belt, while extension occurs simultaneously in the high plateau (Armijo et al., 1986). Tibet therefore represents a more advanced stage of orogen evolution, similar to the Altiplano, in which shortening has localized into the sediments of the foreland basin.



In summary, we suggest that the mechanical properties and nature of the stratigraphy within foreland basins may be important in modulating the forces transmitted across the forelands, the stress field within orogenic belts, and the elevation that mountain belts can attain.

## 6. Conclusions

We have used InSAR, seismology, and field observations to determine a source model for the 1 December 2016  $M_w$  6.1 Parina earthquake in the high Andes of south Peru. Our models suggest that the earthquake was generated by slip on a shallow-crustal normal fault that accommodated NE-SW extension. Slip in the earthquake was partially buried, and around 15–35% of the shallow coseismic slip deficit was accommodated by postseismic afterslip within 6 months of the event.

We find that extension in the Parina earthquake was parallel to the direction of shortening across the adjacent sub-Andean lowlands and that the pattern of shortening in the sub-Andes is controlled by gradients in the topography. In addition, we find that normal faulting earthquakes and geomorphological evidence for recent extensional deformation within the Andes concentrates in regions with the highest elevations. All of these observations imply forces generated by lateral contrasts in gravitational potential energy are important in controlling deformation in the high Andes and its eastern lowlands.

We calculated the force per unit length exerted between the Andes and its forelands due to variations in gravitational potential energy to be  $4\text{--}8 \times 10^{12}$  N/m along strike. Earthquakes within the South American forelands  $> 300$  km from the Andes range front suggest that the crust is breaking in response to these forces, which requires that the foreland faults have an effective coefficient of friction  $\lesssim 0.2$  and support average shear stresses  $\lesssim 110$  MPa. Within 300 km of the Andes range front the extensional stresses in the shallow, bending portion of the foreland lithosphere are large enough to break faults. Using estimates of the curvature of the South American foreland and the rheology of the lithosphere, we can place similar upper bounds on the magnitude of the shear stresses acting on faults in the bending South American forelands ( $\lesssim 90\text{--}130$  MPa).

Normal faulting in the Andes began in the late Miocene following a period of orogen-wide compression, which reflects a change in the force balance across the mountain range. The coeval onset of low-angle detachment faulting in the sub-Andes and extension in the high Andes  $\sim 5\text{--}9$  Ma, in addition to the spatial correlation between extension in the high mountains and wide thin-skinned fold-thrust belts in the adjacent sub-Andes, suggests that weak detachment horizons in the foreland stratigraphy could have reduced the forces transmitted into the mountain belt by shear stresses along the base of the overriding lithosphere, leading to the onset of extension in the high mountains. The dynamics and evolution of the Andes, and we suggest most mountain ranges, may therefore be influenced by the mechanical strength of the stratigraphy in its forelands.

## Appendix A: Derivation of Relaxation Timescale for Elevation Contrasts

Consider two uniform columns of isostatically compensated lithosphere with constant viscosity  $\eta$  and thickness  $L_1$  and  $L_2$  separated by a height difference  $h$ . A simple 1-D horizontal force balance between body forces acting on the columns and viscous resistance, assuming shear stresses on horizontal planes are negligible, is given by (D'Agostino et al., 2012; England & Molnar, 2015)

$$2L \frac{\partial \tau_{xx}}{\partial x} = \frac{\partial \Gamma}{\partial x}, \quad (\text{A1})$$

where  $\tau_{xx}$  is the vertically-averaged horizontal deviatoric stress acting on the columns and  $\Gamma$  is the gravitational potential energy per unit area of each column. Assuming the columns are Newtonian (i.e.,  $\tau_{xx} = 2\eta\dot{\epsilon}_{xx}$ ) and integrating equation (A1) yields

$$\dot{\epsilon}_{xx} = \frac{\Delta \Gamma}{4\eta L}, \quad (\text{A2})$$

where  $\Delta \Gamma$  is the difference in gravitational potential energy between a column with zero strain rate (i.e., undeforming) and the column in question. For Airy isostatic compensation  $\Delta \Gamma$  can be expressed approximately as  $\gamma h$ , where  $\gamma$  is some constant scaling elevation contrasts between the deforming and undeforming area ( $h$ ) to the gravitational potential energy contrast (D'Agostino et al., 2014). In our case, one of the columns (i.e., the Bolivian Altiplano) is assumed to be undeforming; therefore, the strain rate in the deforming column (i.e., south Peru) is proportional to the elevation of that column above the undeforming column.

Assuming incompressibility of each column of lithosphere, and the conservation of area in cross section, horizontal extension of the column at strain rate  $\dot{\epsilon}_{xx}$  in response to horizontal contrasts in gravitational potential energy would lead to thinning given by

$$\frac{dL}{dt} = -\dot{\epsilon}_{xx}L = -\frac{\gamma h}{4\eta} \quad (\text{A3})$$

The difference in the thickness of the higher, deforming column and the undeforming column  $L_1 - L_2$  is related to the elevation contrast through an isostatic relationship  $L_1 - L_2 = h \frac{\rho_m}{\Delta\rho}$ , where  $\Delta\rho$  is the density difference between mantle and crust. Substituting the isostatic relationship into equation (A3) gives the following first-order ordinary differential equation:

$$\frac{dh}{dt} + \frac{\gamma\Delta\rho}{4\eta\rho_m}h = 0 \quad (\text{A4})$$

This equation has a particular solution of the form  $h(t) = h_0 \exp(-t/t_r)$ , where  $t_r = \frac{4\eta\rho_m}{\gamma\Delta\rho}$  and  $h_0$  is the starting elevation of the deforming column above the undeforming column. Therefore, the elevation contrasts between deforming and undeforming regions within a mountain belt will decay exponentially at a rate dependent on the density contrasts between crust and mantle and the viscosity of the lithosphere.

Given the maximum possible extensional strain rate in south Peru as  $2 \times 10^{-8} \text{ year}^{-1}$ ,  $\gamma$  as  $1.5 \times 10^9 \text{ N/m}$  per meter of elevation (see calculations in section 4.1),  $h$  as 700 m, and  $L$  as 150 km, we can use equation (A2) to compute a lower bound on the viscosity, which is  $\eta > 3 \times 10^{21} \text{ Pa s}$ . Our lower bound on the viscosity of the lithosphere is consistent with Lamb (2000), who infer the average viscosity of the lithosphere in the Andes is  $5 - 10 \times 10^{21} \text{ Pa s}$ . Taking  $\rho_m$  and  $\rho_c$  as 3,300 and 2,800  $\text{kg/m}^3$ , respectively, the relaxation timescale of elevation contrasts would be  $t_r > 3 \text{ Myr}$ . Under constant force boundary conditions, after  $>9 \text{ Myr}$  around 95% of the elevation contrasts between south Peru and Bolivia will have been removed via extension. We therefore infer that the elevation contrasts between south Peru and Bolivia are unlikely to have existed for  $>10 \text{ Myr}$ .

## References

- Alvarado, P., & Beck, S. (2006). Source characterization of the San Juan (Argentina) crustal earthquakes of 15 January 1944 (Mw 7.0) and 11 June 1952 (Mw 6.8). *Earth and Planetary Science Letters*, 243, 3–4.
- Armijo, R., Tapponnier, P., Mercier, J. L., & Han, T.-L. (1986). Quaternary extension in southern Tibet: Field observations and tectonic implications. *Journal of Geophysical Research*, 91, 13,803–13,872.
- Artyushkov, E. V. (1973). Stresses in the lithosphere caused by crustal thickness inhomogeneities. *Journal of Geophysical Research*, 78(32), 7675–7708.
- Assumpção, M. (1992). The regional intraplate stress field in South America. *Journal of Geophysical Research*, 97, 11,889–11,903.
- Assumpção, M., & Araujo, M. (1993). Effect of the Altiplano-Puna plateau, South America, on the regional intraplate stresses. *Tectonophysics*, 221(3–4), 475–496.
- Assumpção, M., Feng, M., Tassara, A., & Julià, J. (2013). Models of crustal thickness for South America from seismic refraction, receiver functions and surface wave tomography. *Tectonophysics*, 609, 82–96.
- Assumpção, M., & Suarez, G. (1988). Source mechanisms of moderate-size earthquakes and stress orientation in mid-plate South America. *Geophysical Journal International*, 92(2), 253–267.
- Avouac, J., & Tapponnier, P. (1993). Kinematic model of active deformation in Central Asia. *Geophysical Research Letters*, 20(10), 895–898.
- Babeyko, A. Y., Sobolev, S. V., Vietor, T., Oncken, O., & Trumbull, R. B. (2006). Numerical study of weakening processes in the central Andean back-arc. *The Andes—Active subduction orogeny* (pp. 495–512). Berlin Heidelberg: Springer.
- Barke, R., & Lamb, S. (2006). Late Cenozoic uplift of the Eastern Cordillera, Bolivian Andes. *Earth and Planetary Science Letters*, 249(3–4), 350–367.
- Beck, S. L., & Zandt, G. (2002). The nature of orogenic crust in the central Andes. *Journal of Geophysical Research*, 107(B10), 2230.
- Benavente, E. C., Delgado, M. F., Taipe, M. E., Audin, L., & Pari, W. (2013). Neotectonica y Peligro Sísmico en el Region Cusco (Technical report). Lima, Perú: Instituto Geológico Minera y Metalúrgico.
- Benavente, C., Zerathe, S., Audin, L., Hall, S. R., Robert, X., Delgado, F., et al. (2017). Active transpressional tectonics in the Andean forearc of southern Peru quantified by  $^{10}\text{Be}$  surface exposure dating of an active fault scarp. *Tectonics*, 36, 1662–1678. <https://doi.org/10.1002/2017TC004523>
- Bevis, M., Kendrick, E., Smalley, R., Brooks, B., Allmendinger, R., & Isacks, B. (2001). On the strength of interplate coupling and the rate of back arc convergence in the central Andes: An analysis of the interseismic velocity field. *Geochemistry, Geophysics, Geosystems*, 2(11), 1067.
- Bevis, M., & Martel, S. J. (2001). Oblique plate convergence and interseismic strain accumulation. *Geochemistry, Geophysics, Geosystems*, 8, 1033.
- Bie, L., Ryder, I., Nippress, S. E. J., & Burgmann, R. (2014). Coseismic and post-seismic activity associated with the 2008  $M_w$  6.3 Damxung earthquake, Tibet, constrained by InSAR. *Geophysical Journal International*, 196(2), 788–803.
- Bouhifd, M. a., Andrault, D., Fiquet, G., & Richet, P. (1996). Thermal expansion of forsterite up to the melting point. *Geophysical Research Letters*, 23(10), 1143–1146.
- Brace, W. F., & Kohlstedt, D. L. (1980). Limits on lithospheric stress imposed by laboratory experiments. *Journal of Geophysical Research*, 85(B11), 6248–6252.
- Brune, J. N. (1968). Seismic moment, seismicity, and rate of slip along major fault zones. *Journal of Geophysical Research*, 73(2), 777–784.
- Bry, M., & White, N. (2007). Reappraising elastic thickness variation at oceanic trenches. *Journal of Geophysical Research*, 112, B08414. <https://doi.org/10.1029/2005JB004190>

## Acknowledgments

This work forms part of the NERC- and ESRC-funded project *Earthquakes without Frontiers* and was partly supported by the NERC large grant *Looking into Continents from Space*. C. B. and E. A. wish to acknowledge INGEMMET and Cusco-PATA (Nú006-2016-FONDECYT) for support of the fieldwork. S. W. was partly supported by the British Geological Survey. S. W. thanks Marcelo Assumpção for providing the crustal thickness measurements, in addition to Lorcan Kennan, Christoph Grützner, and James Jackson for discussions. The authors thank Peter Molnar, Robert Smalley, and particularly Simon Lamb for constructive reviews. Figures were drafted using the free software Generic Mapping Tools (Wessel et al., 2013). All data used in this study are open access and freely available. InSAR data were collected from the ESA Copernicus Hub (<https://scihub.copernicus.eu/>), seismic data were downloaded from the IRIS data management center ([http://ds.iris.edu/wilber3/find\\_event/](http://ds.iris.edu/wilber3/find_event/)), and Landsat data were collected from EarthExplorer (<https://earthexplorer.usgs.gov/>).

- Byerlee, J. (1978). Friction of rocks. *Pure and Applied Geophysics*, 116(4-5), 615–626.
- Cabrera, J., & Sebrier, M. (1998). Surface rupture associated with a 5.3-mb earthquake: The 5 April 1986 Cuzco earthquake and kinematics of the Chincheros-Qoricocha Faults of the High Andes, Peru. *Bulletin of the Seismological Society of America*, 88(1), 242–255.
- Cabrera, J., Sébrier, M., & Mercier, J. L. (1991). Plio-Quaternary geodynamic evolution of a segment of the Peruvian Andean Cordillera located above the change in the subduction geometry: The Cuzco region. *Tectonophysics*, 190(2-4), 331–362.
- Chapman, C. H. (1978). A new method for computing synthetic seismograms. *Geophysical Journal International*, 54(3), 481–518.
- Chen, C. W., & Zebker, H. A. (2001). Two-dimensional phase unwrapping with use of statistical models for cost functions in nonlinear optimization. *Journal of the Optical Society of America A*, 18(2), 338–51.
- Chinn, D. S., & Isacks, B. L. (1983). Accurate source depths and focal mechanisms of shallow earthquakes in western South America and in the New Hebrides Island Arc. *Tectonics*, 2(6), 529–563.
- Chlieh, M., Perfettini, H., Tavera, H., Avouac, J.-P., Remy, D., Nocquet, J.-M., et al. (2011). Interseismic coupling and seismic potential along the Central Andes subduction zone. *Journal of Geophysical Research*, 116, B12405. <https://doi.org/10.1029/2010JB008166>
- Cladouhos, T. T., Allmendinger, R. W., Coira, B., & Farrar, E. (1994). Late Cenozoic deformation in the Central Andes: Fault kinematics from the northern Puna, northwestern Argentina and southwestern Bolivia. *Journal of South American Earth Sciences*, 7(2), 209–228.
- Clapperton, C. (1983). The glaciation of the Andes. *Quaternary Science Reviews*, 2(2-3), 83–155.
- Collettini, C., Niemeijer, A., Viti, C., & Marone, C. (2009). Fault zone fabric and fault weakness. *Nature*, 462(7275), 907–910.
- Copley, A. (2012). The formation of mountain range curvature by gravitational spreading. *Earth and Planetary Science Letters*, 351-352, 208–214.
- Copley, A., Avouac, J.-P., Hollingsworth, J., & Leprince, S. (2011). The 2001  $M_w$  7.6 Bhuj earthquake, low fault friction, and the crustal support of plate driving forces in India. *Journal of Geophysical Research*, 116, B08405. <https://doi.org/10.1029/2010JB008137>
- Copley, A., Avouac, J.-P., & Wernicke, B. P. (2011). Evidence for mechanical coupling and strong Indian lower crust beneath southern Tibet. *Nature*, 472(7341), 79–81.
- Copley, A., Boait, F., Hollingsworth, J., Jackson, J., & McKenzie, D. (2009). Subparallel thrust and normal faulting in Albania and the roles of gravitational potential energy and rheology contrasts in mountain belts. *Journal of Geophysical Research*, 114, B05407. <https://doi.org/10.1029/2008JB005931>
- Copley, A., Karasozen, E., Oveisi, B., Elliott, J. R., Samsonov, S., & Nissen, E. (2015). Seismogenic faulting of the sedimentary sequence and laterally variable material properties in the Zagros Mountains (Iran) revealed by the August 2014 Murmuri (E. Dehloran) earthquake sequence. *Geophysical Journal International*, 203(2), 1436–1459.
- Copley, A., & McKenzie, D. (2007). Models of crustal flow in the India-Asia collision zone. *Geophysical Journal International*, 169(2), 683–698.
- Copley, A., & Woodcock, N. (2016). Estimates of fault strength from the Variscan foreland of the northern UK. *Earth and Planetary Science Letters*, 451, 108–113.
- Craig, T. J., & Copley, A. (2018). Forearc collapse, plate flexure, and seismicity within the downgoing plate along the Sunda Arc west of Sumatra. *Earth and Planetary Science Letters*, 484, 81–91.
- Craig, T. J., Copley, A., & Jackson, J. (2012). Thermal and tectonic consequences of India underthrusting Tibet. *Earth and Planetary Science Letters*, 353-354, 231–239.
- Craig, T. J., Jackson, J. a., Priestley, K., & McKenzie, D. (2011). Earthquake distribution patterns in Africa: Their relationship to variations in lithospheric and geological structure, and their rheological implications. *Geophysical Journal International*, 185(1), 403–434.
- D'Agostino, N., Cheloni, D., Fornaro, G., Giuliani, R., & Reale, D. (2012). Space-time distribution of afterslip following the 2009 L'Aquila earthquake. *Journal of Geophysical Research*, 117, B02402. <https://doi.org/10.1029/2011JB008523>
- D'Agostino, N., England, P., Hunstad, I., & Selvaggi, G. (2014). Gravitational potential energy and active deformation in the Apennines. *Earth and Planetary Science Letters*, 397, 121–132.
- Dalmayrac, B., & Molnar, P. (1981). Parallel thrust and normal faulting in Peru and constraints on the state of stress. *Earth and Planetary Science Letters*, 55(3), 473–481.
- Daxberger, H., & Riller, U. (2015). Kinematics of Neogene to Recent upper-crustal deformation in the southern Central Andes (23-28S) inferred from fault-slip analysis: Evidence for gravitational spreading of the Puna Plateau. *Tectonophysics*, 642(1), 16–28.
- DeMets, C., Gordon, R. G., & Argus, D. F. (2010). Geologically current plate motions. *Geophysical Journal International*, 181(1), 1–80.
- Devlin, S., Isacks, B. L., Pritchard, M. E., Barnhart, W. D., & Lohman, R. B. (2012). Depths and focal mechanisms of crustal earthquakes in the central Andes determined from teleseismic waveform analysis and InSAR. *Tectonics*, 31, TC2002. <https://doi.org/10.1029/2011TC002914>
- Dorbath, C. (1996). Velocity structure of the Andes of central Peru from locally recorded earthquakes. *Geophysical Research Letters*, 23(2), 205–208.
- Doser, D. I. (1987). The Ancash, Peru, earthquake of 1946 November 10: Evidence for low-angle normal faulting in the high Andes of northern Peru. *Geophysical Journal of the Royal Astronomical Society*, 91(1), 57–71.
- Dziewonski, A. M., Chou, T.-A., & Woodhouse, J. H. (1981). Determination of earthquake source parameters from waveform data for studies of global and regional seismicity. *Journal of Geophysical Research*, 86(B4), 2825–2852.
- Echavarría, L., Hernández, R., Allmendinger, R., & Reynolds, J. (2003). Subandean thrust and fold belt of northwestern Argentina: Geometry and timing of the Andean evolution. *AAPG Bulletin*, 87(6), 965–985.
- Ekström, G., Nettles, M., & Dziewoński, A. (2012). The global CMT project 2004–2010: Centroid-moment tensors for 13,017 earthquakes. *Physics of the Earth and Planetary Interiors*, 200, 1–9.
- Elger, K., Oncken, O., & Glodny, J. (2005). Plateau-style accumulation of deformation: Southern Altiplano. *Tectonics*, 24, TC4020. <https://doi.org/10.1029/2004TC001675>
- Ellison, R., Klinck, B., & Hawkins, M. (1989). Deformation events in the Andean orogenic cycle in the Altiplano and Western Cordillera, southern Peru. *Journal of South American Earth Sciences*, 2(3), 263–276.
- Emmerson, B. (2007). The relationship between intraplate earthquakes and temperature (PhD thesis), University of Cambridge.
- Engdahl, E. R., van der Hilst, R., & Buland, R. (1998). Global teleseismic earthquake relocation with improved travel times and procedures for depth determination. *Bulletin of the Seismological Society of America*, 88(3), 722–743.
- England, P., & Houseman, G. (1989). Extension during continental convergence, with application to the Tibetan Plateau. *Journal of Geophysical Research*, 94(B12), 17,561–17,579.
- England, P., & McKenzie, D. (1982). A thin viscous sheet model for continental deformation. *Geophysical Journal International*, 70(2), 295–321.
- England, P., & Molnar, P. (1997). Active deformation of Asia: From kinematics to dynamics. *Science*, 278(5338).
- England, P., & Molnar, P. (2015). Rheology of the lithosphere beneath the central and western Tien Shan. *Journal of Geophysical Research: Solid Earth*, 120, 3803–3823. <https://doi.org/10.1002/2014JB011733>

- Espurt, N., Brusset, S., Baby, P., Hermoza, W., Bolaños, R., Uyen, D., & Déramond, J. (2008). Paleozoic structural controls on shortening transfer in the Subandean foreland thrust system, Ene and southern Ucayali basins, Peru. *Tectonics*, 27, TC3009. <https://doi.org/10.1029/2007TC002238>
- Farr, T. G., Rosen, P. A., Caro, E., Crippen, R., Duren, R., Hensley, S., et al. (2007). The Shuttle Radar Topography Mission. *Reviews of Geophysics*, 45(2), RG2004.
- Fialko, Y., Sandwell, D., Simons, M., & Rosen, P. (2005). Three-dimensional deformation caused by the Bam, Iran, earthquake and the origin of shallow slip deficit. *Nature*, 435(7040), 295–299.
- Fielding, E. J., Lundgren, P. R., Bürgmann, R., & Funning, G. J. (2009). Shallow fault-zone dilatancy recovery after the 2003 Bam earthquake in Iran. *Nature*, 458(7234), 64–68.
- Flesch, L. M., & Kreemer, C. (2010). Gravitational potential energy and regional stress and strain rate fields for continental plateaus: Examples from the central Andes and Colorado Plateau. *Tectonophysics*, 482(1-4), 182–192.
- Froidevaux, C., & Isacks, B. L. (1984). The mechanical state of the lithosphere in the Altiplano-Puna segment of the Andes. *Earth and Planetary Science Letters*, 71(2), 305–314.
- Funning, G. J., Barke, R. M. D., Lamb, S. H., Minaya, E., Parsons, B., & Wright, T. J. (2005). The 1998 Aiquile, Bolivia earthquake: A seismically active fault revealed with InSAR. *Earth and Planetary Science Letters*, 232(1-2), 39–49.
- Garzzone, C. N., Hoke, G. D., Libarkin, J. C., Withers, S., MacFadden, B., Eiler, J., et al. (2008). Rise of the Andes. *Science (New York, N.Y.)*, 320(5881), 1304–1307.
- Garzzone, C. N., McQuarrie, N., Perez, N. D., Ehlers, T. A., Beck, S. L., Kar, N., et al. (2017). Tectonic evolution of the Central Andean Plateau and implications for the growth of plateaus. *Annual Review of Earth and Planetary Sciences*, 45(1), 529–559.
- Garzzone, C. N., Molnar, P., Libarkin, J. C., & MacFadden, B. J. (2006). Rapid late Miocene rise of the Bolivian Altiplano: Evidence for removal of mantle lithosphere. *Earth and Planetary Science Letters*, 241(3-4), 543–556.
- Gautheron, C., Espurt, N., Barbarand, J., Roddaz, M., Baby, P., Brusset, S., et al. (2013). Direct dating of thick- and thin-skin thrusts in the Peruvian Subandean zone through apatite (U-Th)/He and fission track thermochronometry. *Basin Research*, 25(4), 419–435.
- Giovanni, M. K., Horton, B. K., Garzzone, C. N., McNulty, B., & Grove, M. (2010). Extensional basin evolution in the Cordillera Blanca, Peru: Stratigraphic and isotopic records of detachment faulting and orogenic collapse in the Andean hinterland. *Tectonics*, 29, TC6007. <https://doi.org/10.1029/2010TC002666>
- Goetze, C., & Evans, B. (1979). Stress and temperature in the bending lithosphere as constrained by experimental rock mechanics. *Geophysical Journal of the Royal Astronomical Society*, 59(3), 463–478.
- Goldstein, R. M., Zebker, H. A., & Werner, C. L. (1988). Satellite radar interferometry: Two-dimensional phase unwrapping. *Radio Science*, 23(4), 713–720.
- Gubbels, T. L., Isacks, B. L., & Farrar, E. (1993). High-level surfaces, plateau uplift, and foreland development, Bolivian central Andes. *Geology*, 21(8), 695–698.
- Gutscher, M.-A., Spakman, W., Bjiwaard, H., & Enghdahl, E. R. (2000). Geodynamics of flat subduction: Seismicity and tomographic constraints from the Andean margin. *October*, 19(5), 814–833.
- Hall, S. R., Farber, D. L., Audin, L., & Finkel, R. C. (2012). Recently active contractile deformation in the forearc of southern Peru. *Earth and Planetary Science Letters*, 337-338, 85–92.
- Heim, A. (1946). Observaciones Geologicas en La Region del Terremoto de Ancash de Noviembre de (Technical Report) Lima, Peru: Sociada Geologica del Peru.
- Hoke, L., & Lamb, S. (2007). Cenozoic behind-arc volcanism in the Bolivian Andes, South America: Implications for mantle melt generation and lithospheric structure. *Journal of the Geological Society*, 164(4), 795–814.
- Holtkamp, S. G., Pritchard, M. E., & Lohman, R. B. (2011). Earthquake swarms in South America. *Geophysical Journal International*, 187(1), 128–146.
- Huppert, H. E. (1982). Propagation of two-dimensional and axisymmetric viscous gravity currents over a rigid horizontal surface. *Journal of Fluid Mechanics*, 121, 43–58.
- Husson, L., & Ricard, Y. (2004). Stress balance above subduction: Application to the Andes. *Earth and Planetary Science Letters*, 222(3-4), 1037–1050.
- Imber, J., Holdsworth, R. E., Smith, S. A. F., Jefferies, S. P., & Colletini, C. (2008). Frictional-viscous flow, seismicity and the geology of weak faults: A review and future directions. *Geological Society, London, Special Publications*, 299(1), 151–173.
- Ingleby, T., & Wright, T. J. (2017). Omorilike decay of postseismic velocities following continental earthquakes. *Geophysical Research Letters*, 44, 3119–3130. <https://doi.org/10.1002/2017GL072865>
- Jackson, M., & Blenkinsop, T. (1997). The Bilila-Mtakataka fault in Malai: An active, 100-km long, normal fault segment in thick seismogenic crust. *Tectonics*, 16(1), 137–150.
- Jackson, J. A. J., Gagnepain, J., Houseman, G., King, G. C. P., Papadimitriou, P., Soufleris, C., & Viriueux, J. (1982). Seismicity, normal faulting, and the geomorphological development of the Gulf of Corinth (Greece): The Corinth earthquakes of February and March 1981. *Earth and Planetary Science Letters*, 57(2), 377–397.
- Jackson, J., McKenzie, D., Priestley, K., & Emmerson, B. (2008). New views on the structure and rheology of the lithosphere. *Journal of the Geological Society*, 165(2), 453–465.
- Jackson, J., Priestley, K., Allen, M., & Berberian, M. (2002). Active tectonics of the South Caspian Basin. *Geophysical Journal International*, 148(2), 214–245.
- Jackson, J. A., & White, N. J. (1989). Normal faulting in the upper continental crust: Observations from regions of active extension. *Journal of Structural Geology*, 11(1-2), 15–36.
- Jay, J. A., Delgado, F. J., Torres, J. L., Pritchard, M. E., Macedo, O., & Aguilar, V. (2015). Deformation and seismicity near Sabancaya volcano, southern Peru, from 2002 to 2015. *Geophysical Research Letters*, 42, 2780–2788. <https://doi.org/10.1002/2015GL063589>
- Kadinsky-Cade, K., Reilinger, R., & Isacks, B. (1985). Surface deformation associated with the November 23, 1977, Caucete, Argentina, earthquake sequence. *Journal of Geophysical Research*, 90, 12691–12700.
- Kaneko, Y., & Fialko, Y. (2011). Shallow slip deficit due to large strike-slip earthquakes in dynamic rupture simulations with elasto-plastic off-fault response. *Geophysical Journal International*, 186(3), 1389–1403.
- Kar, N., Garzzone, C. N., Jaramillo, C., Shanahan, T., Carlotto, V., Pullen, A., et al. (2016). Rapid regional surface uplift of the northern Altiplano plateau revealed by multiproxy paleoclimate reconstruction. *Earth and Planetary Science Letters*, 447, 33–47.
- Karato, S.-i., & Wu, P. (1993). Rheology of the upper mantle: A synthesis. *Science*, 260(5109), 771–778.
- Kay, R., & Mahlburg Kay, S. (1993). Delamination and delamination magmatism. *Tectonophysics*, 219(1-3), 177–189.
- Kendrick, E., Bevis, M., & Brooks, B. (2001). An integrated crustal velocity field for the central Andes. *Geochemistry, Geophysics, Geosystems*, 11, 1066.

- Kennan, L. (1993). Cenozoic evolution of the Cochabamba Area, Bolivia. In *Second ISAG* (pp. 21–23). Oxford, UK.
- Kennett, B. L. N., Engdahl, E. R., & Buland, R. (1995). Constraints on seismic velocities in the Earth from traveltimes. *Geophysical Journal International*, *122*(1), 108–124.
- Kley, J. (1996). Transition from basement-involved to thin-skinned thrusting in the Cordillera Oriental of southern Bolivia. *Tectonics*, *15*(4), 763–775.
- Kley, J., & Monaldi, C. R. (1998). Tectonic shortening and crustal thickness in the Central Andes: How good is the correlation *Geology*, *26*(8), 723–726.
- Kley, J., Monaldi, C. R., & Salfity, J. A. (1999). Along-strike segmentation of the Andean foreland: Causes and consequences. *Tectonophysics*, *301*(1–2), 75–94.
- Kober, M., Seib, N., Kley, J., & Voigt, T. (2013). Thick-skinned thrusting in the northern Tien Shan foreland, Kazakhstan: Structural inheritance and polyphase deformation. *Geological Society, London, Special Publications*, *377*(1), 19–42.
- Lamb, S. H. (2000). Active deformation in the Bolivian Andes, South America. *Journal of Geophysical Research*, *105*(B11), 25627–25653.
- Lamb, S. (2006). Shear stresses on megathrusts: Implications for mountain building behind subduction zones. *Journal of Geophysical Research*, *111*, B07401. <https://doi.org/10.1029/2005JB003916>
- Lamb, S. (2011). Did shortening in thick crust cause rapid Late Cenozoic uplift in the northern Bolivian Andes *Journal of the Geological Society*, *168*(5), 1079–1092.
- Lamb, S. (2016). Cenozoic uplift of the Central Andes in northern Chile and Boliviareconciling paleoaltimetry with the geological evolution. *Canadian Journal of Earth Sciences*, *53*(11), 1227–1245.
- Lamb, S., & Hoke, L. (1997). Origin of the high plateau in the Central Andes, Bolivia, South America. *Journal of Geophysical Research*, *16*(4), 623–649.
- Lavé, J., & Avouac, J. P. (2000). Active folding of fluvial terraces across the Siwaliks Hills, Himalayas of central Nepal. *Journal of Geophysical Research*, *105*(B3), 5735–5770.
- Lavenu, A., Thiele, R., Machette, M., Dart, R., Lee-Ann, B., & Haller, K. (2000). Maps and database of Quaternary faults in Bolivia and Chile (*Technical report*). Paris, France: United States Geological Survey.
- Lin, Y. N. N., Sladen, A., Ortega-Culaciati, F., Simons, M., Avouac, J. P., Fielding, E. J., et al. (2013). Coseismic and postseismic slip associated with the 2010 Maule Earthquake, Chile: Characterizing the Arauco Peninsula barrier effect. *Journal of Geophysical Research: Solid Earth*, *118*, 3142–3159. <https://doi.org/10.1002/jgrb.50207>
- Liu, M., Yang, Y., Stein, S., & Klosko, E. (2002). Crustal shortening and extension in the Central Andes: Insights from a viscoelastic model. *AGU Geodynamics Series*, *30*, 325–339.
- Lucassen, F., Franz, G., Viramonte, J., Romer, R. L., Dulski, P., & Lang, A. (2005). The late Cretaceous lithospheric mantle beneath the Central Andes: Evidence from phase equilibria and composition of mantle xenoliths. *Lithos*, *82*(3–4 SPEC. ISS.), 379–406.
- Lucassen, F., Lewerenz, S., Franz, G., Viramonte, J., & Mezger, K. (1999). Metamorphism, isotopic ages and composition of lower crustal granulite xenoliths from the Cretaceous Salta Rift, Argentina. *Contributions to Mineralogy and Petrology*, *134*(4), 325–341.
- Lyon-Caen, H., Molnar, P., & Suárez, G. (1985). Gravity anomalies and flexure of the Brazilian Shield beneath the Bolivian Andes. *Earth and Planetary Science Letters*, *75*(1), 81–92.
- Maggi, A., Jackson, J. A., McKenzie, D., & Priestley, K. (2000). Earthquake focal depths, effective elastic thickness, and the strength of the continental lithosphere. *Geology*, *28*(6), 495–498.
- Maggi, A., Jackson, J. A., Priestley, K., & Baker, C. (2000). A re-assessment of focal depth distributions in southern Iran, the Tien Shan and northern India: Do earthquakes really occur in the continental mantle *Geophysical Journal International*, *143*(3), 629–661.
- Margjirier, A., Audin, L., Robert, X., Pècher, A., & Schwartz, S. (2017). Stress field evolution above the Peruvian flat-slab (Cordillera Blanca, northern Peru). *Journal of South American Earth Sciences*, *77*, 58–69.
- Marone, C., & Scholz, C. H. (1988). The depth of seismic faulting and the upper transition from stable to unstable slip regimes. *Geophysical Research Letters*, *15*(6), 621–624.
- Marrett, R. A., Allmendinger, R. W., Alonso, R. N., & Drake, R. E. (1994). Late Cenozoic tectonic evolution of the Puna Plateau and adjacent foreland, northwestern Argentine Andes. *Journal of South American Earth Sciences*, *7*(2), 179–207.
- McCaffrey, R., & Abers, G. (1988). Syn3: A program for inversion of teleseismic body waveforms on microcomputers.
- McCaffrey, R., Abers, G., & Zwick, A. (1991). Inversion of teleseismic body waves, in *Digital Seismogram Analysis and Waveform Inversion*. W. Lee (ed.), *IASPEI Software Library*, chapter 3: IASPEI Software Library, Vol. 3, Menlo Park, USA.
- McGroder, M. F., Lease, R. O., & Pearson, D. M. (2015). Along-strike variation in structural styles and hydrocarbon occurrences, Subandean fold-and-thrust belt and inner foreland, Colombia to Argentina. In P. G. DeCelles, et al. (Eds.), *Geodynamics of a Cordilleran Orogenic System: The Central Andes of Argentina and Northern Chile*: Geological Society of America Memoir, 212.
- McKenzie, D., & Fairhead, D. (1997). Estimates of the effective elastic thickness of the continental lithosphere from Bouguer and free air gravity anomalies. *Journal of Geophysical Research*, *102*(B12), 27523–27552.
- McKenzie, D., Jackson, J., & Priestley, K. (2005). Thermal structure of oceanic and continental lithosphere. *Earth and Planetary Science Letters*, *233*(3), 337–349.
- McKenzie, D., Nimmo, F., & Jackson, J. A. (2000). Characteristics and consequences of flow in the lower crust. *Journal of Geophysical Research*, *105*(B5), 11029–11046.
- McKenzie, D. P., & Parker, R. L. (1967). The North Pacific: An example of tectonics on a sphere. *Nature*, *216*(5122), 1276–1280.
- McKenzie, D., & Priestley, K. (2008). The influence of lithospheric thickness variations on continental evolution. *Lithos*, *102*(1–2), 1–11.
- McKenzie, D., & Priestley, K. (2016). Speculations on the formation of cratons and cratonic basins. *Earth and Planetary Science Letters*, *435*, 94–104.
- McKenzie, D., Yi, W., & Rummel, R. (2014). Estimates of  $T_e$  from GOCE Data. *Earth and Planetary Science Letters*, *399*, 116–127.
- McNulty, B., & Farber, D. (2002). Active detachment faulting above the Peruvian flat slab. *Geology*, *30*(6), 567–570.
- Megard, F., Noble, D., McKee, E., & Bellon, H. (1984). Multiple pulses of Neogene compressive deformation in the Ayacucho intermontane basin, Andes of central Peru. *Geological Society of America Bulletin*, *95*(9), 1108–1117.
- Mei, S., Suzuki, A. M., Kohlstedt, D. L., Dixon, N. A., & Durham, W. B. (2010). Experimental constraints on the strength of the lithospheric mantle. *Journal of Geophysical Research*, *115*, B08204. <https://doi.org/10.1029/2009JB006873>
- Meijer, P., Govers, R., & Wortel, M. (1997). Forces controlling the present-day state of stress in the Andes. *Earth and Planetary Science Letters*, *148*(1–2), 157–170.
- Mercier, J. L. (1981). Extensional-compressional tectonics associated with the Aegean Arc: Comparison with the Andean Cordillera of South Peru-North Bolivia. *Philosophical Transactions of the Royal Society of London A: Mathematical, Physical and Engineering Sciences*, *300*(1454), 337–355.

- Mercier, J. L., Sebrier, M., Lavenu, A., Cabrera, J., Bellier, O., Dumont, J.-F., & Machrare, J. (1992). Changes in the tectonic regime above a subduction zone of Andean Type: The Andes of Peru and Bolivia during the Pliocene-Pleistocene. *Journal of Geophysical Research*, *97*(B8), 11945.
- Molnar, P., Chen, W.-P., Fitch, T. J., Tapponnier, P., Warsi, W. E. K., & Wu, F. (1977). Structure and tectonics of the Himalaya: A brief summary of relevant geophysical observations. In *Colloque International du CNRS, No. 268, Himalaya: Sciences de la Terre*, Paris. du Centre National de la Recherche Scientifique, pp. 269–294.
- Molnar, P., & Lyon-Caen, H. (1988). Some simple physical aspects of the support, structure, and evolution of mountain belts, *Geological Society of America Special Papers* (Vol. 218, pp. 179–208). Boulder, Colorado, USA: Geological Society of America.
- Molnar, P., & Lyon-Caen, H. (1989). Fault plane solutions of earthquakes and active tectonics of the Tibetan Plateau and its margins. *Geophysical Journal International*, *99*(1), 123–154.
- Molnar, P., & Stock, J. M. (2009). Slowing of India's convergence with Eurasia since 20 Ma and its implications for Tibetan mantle dynamics. *Tectonics*, *28*, TC3001. <https://doi.org/10.1029/2008TC002271>
- Montero Lopez, M. C., Hongn, F. D., Strecker, M. R., Marrett, R., Seggiano, R., & Sudo, M. (2010). Late Miocene-early Pliocene onset of N-S extension along the southern margin of the Central Andean Puna Plateau: Evidence from magmatic, geochronological and structural observations. *Tectonophysics*, *494*(1-2), 48–63.
- Nemati, M., Hollingsworth, J., Zhan, Z., Bolourchi, M. J., & Talebian, M. (2013). Microseismicity and seismotectonics of the South Caspian Lowlands, NE Iran. *Geophysical Journal International*, *193*(3), 1053–1070.
- Ni, J., & Barazangi, M. (1984). Seismotectonics of the Himalayan Collision Zone: Geometry of the underthrusting Indian Plate beneath the Himalaya. *Journal of Geophysical Research*, *89*(B2), 1147–1163.
- Norabuena, E. O., Dixon, T. H., Stein, S., & Harrison, C. G. A. (1999). Decelerating Nazca-South America and Nazca-Pacific Plate motions. *Geophysical Research Letters*, *26*(22), 3405–3408.
- Okada, Y. (1985). Surface deformation due to shear and tensile faults in a half-space. *Bulletin of the Seismological Society of America*, *75*(4), 1135–1154.
- Oncken, O., Boutelier, D., Dresen, G., & Schemmann, K. (2012). Strain accumulation controls failure of a plate boundary zone: Linking deformation of the Central Andes and lithosphere mechanics. *Geochemistry, Geophysics, Geosystems*, *13*, Q12007. <https://doi.org/10.1029/2012GC004280>
- Oncken, O., Hindle, D., Kley, J., Elger, K., Victor, P., & Schemmann, K. (2006). Deformation of the Central Andean Upper Plate System facts, fiction, and constraints for plateau models, *The Andes* (pp. 3–27). Berlin Heidelberg: Springer.
- Peltzer, G., Rosen, P., Rogez, F., & Hudnut, K. (1998). Poroelastic rebound along the Landers 1992 earthquake surface rupture. *Journal of Geophysical Research*, *103*(B12), 30,131–30,145.
- Perez, N., Horton, B., McQuarrie, N., Stubner, K., & Ehlers, T. (2016). Andean shortening, inversion and exhumation associated with thin- and thick-skinned deformation in southern Peru. *Geological Magazine*, *153*(5-6), 1013–1041.
- Pérez-Gussinyé, M., Lowry, A. R., & Watts, A. B. (2007). Effective elastic thickness of South America and its implications for intracontinental deformation. *Geochemistry, Geophysics, Geosystems*, *8*, Q05009. <https://doi.org/10.1029/2006GC001511>
- Philip, H., & Megard, F. (1977). Structural analysis of the superficial deformation of the 1969 Paríhuanca earthquakes (Central Peru). *Tectonophysics*, *38*(3-4), 259–278.
- Phillips, K., Clayton, R. W., Davis, P., Tavera, H., Guy, R., Skinner, S., et al. (2012). Structure of the subduction system in southern Peru from seismic array data. *Journal of Geophysical Research*, *117*, B11306. <https://doi.org/10.1029/2012JB009540>
- Priestley, K., & McKenzie, D. (2013). The relationship between shear wave velocity, temperature, attenuation and viscosity in the shallow part of the mantle. *Earth and Planetary Science Letters*, *381*, 78–91.
- Pritchard, M. E., Norabuena, E. O., Ji, C., Boroschek, R., Comte, D., Simons, M., et al. (2007). Geodetic, teleseismic, and strong motion constraints on slip from recent southern Peru subduction zone earthquakes. *Journal of Geophysical Research*, *112*, B03307. <https://doi.org/10.1029/2006JB004294>
- Renner, S., & Velasco, C. (2000). Geología E Hidrogeología Del Valle Central De Cochabamba (Technical Report). Cochabamba, Bolivia: German Bolivian Agreement on Groundwater (CABAS).
- Reynolds, K., Copley, a., & Hussain, E. (2015). Evolution and dynamics of a fold-thrust belt: The Sulaiman Range of Pakistan. *Geophysical Journal International*, *201*(2), 683–710.
- Riller, U., Clark, M. D., Daxberger, H., Doman, D., Lenauer, I., Plath, S., & Santimano, T. (2017). Fault-slip inversions: Their importance in terms of strain, heterogeneity, and kinematics of brittle deformation. *Journal of Structural Geology*, *101*, B2–B6.
- Rodríguez Tribaldos, V., White, N. J., Roberts, G. G., & Hoggard, M. J. (2017). Spatial and temporal uplift history of South America from calibrated drainage analysis. *Geochemistry, Geophysics, Geosystems*, *18*, 2321–2353. <https://doi.org/10.1002/2017GC006909>
- Savage, J. C., Svarc, J. L., & Yu, S.-B. (2005). Postseismic relaxation and transient creep. *Journal of Geophysical Research*, *110*, B11402. <https://doi.org/10.1029/2005JB003687>
- Saylor, J. E., & Horton, B. K. (2014). Nonuniform surface uplift of the Andean plateau revealed by deuterium isotopes in Miocene volcanic glass from southern Peru. *Earth and Planetary Science Letters*, *387*, 120–131.
- Schoenbohm, L. M., & Strecker, M. R. (2009). Normal faulting along the southern margin of the Puna Plateau, northwest Argentina. *Tectonics*, *28*, TC5008. <https://doi.org/10.1029/2008TC002341>
- Scholz, C. H. (1998). Earthquakes and friction laws. *Nature*, *391*(6662), 37–42.
- Scholz, C. H. (2002). *The mechanics of earthquakes and faulting*. Cambridge, UK: Cambridge University Press.
- Schurr, B., Asch, G., Rietbrock, A., Kind, R., Pardo, M., Heit, B., & Monfret, T. (1999). Seismicity and average velocities beneath the Argentine Puna Plateau. *Geophysical Research Letters*, *26*(19), 3025–3028.
- Scott, C., Lohman, R., Pritchard, M., Alvarado, P., & Sánchez, G. (2014). Andean earthquakes triggered by the 2010 Maule, Chile (Mw8.8) earthquake: Comparisons of geodetic, seismic and geologic constraints. *Journal of South American Earth Sciences*, *50*, 27–39.
- Sébrier, M., Mercier, J. L., Macharé, J., Bonnot, D., Cabrera, J., & Blanc, J. L. (1988). The state of stress in an overriding plate situated above a flat slab: The Andes of central Peru. *Tectonics*, *7*(4), 895–928.
- Sébrier, M., Mercier, J. L., Mégard, F., Laubacher, G., & Carey-Gailhardis, E. (1985). Quaternary normal and reverse faulting and the state of stress in the central Andes of south Peru. *Tectonics*, *4*(7), 739–780.
- Shako, R., Forste, C., Abrikosov, O., Bruinsma, S., Marty, J.-C., Lemoine, J.-M., et al. (2014). EIGEN-6C: A High-resolution global gravity combination model including GOCE data. *Observation of the System Earth from Space - CHAMP, GRACE, GOCE and future missions*, 155–161.
- Sibson, R. H. (2004). Controls on maximum fluid overpressure defining conditions for mesozonal mineralisation. *Journal of Structural Geology*, *26*(6-7), 1127–1136.

- Sladen, A., Tavera, H., Simons, M., Avouac, J. P., Konca, A. O., Perfettini, H., et al. (2010). Source model of the 2007  $M_w$  8.0 Pisco, Peru earthquake: Implications for seismogenic behavior of subduction megathrusts. *Journal of Geophysical Research*, *115*, B02405. <https://doi.org/10.1029/2009JB006429>
- Sloan, R. A., Jackson, J. A., McKenzie, D., & Priestley, K. (2011). Earthquake depth distributions in central Asia, and their relations with lithosphere thickness, shortening and extension. *Geophysical Journal International*, *185*(1), 1–29.
- Smith, J. A., Seltzer, G. O., Rodbell, D. T., & Klein, A. G. (2005). Regional synthesis of last glacial maximum snowlines in the tropical Andes, South America. *Quaternary International*, *138–139*, 145–167.
- Smith, S. W., & Wyss, M. (1968). Displacement on the San Andreas fault subsequent to the 1966 Parkfield earthquake. *Bulletin of the Seismological Society of America*, *58*(6), 1955–1973.
- Stewart, J., & Watts, A. B. (1997). Gravity anomalies and spatial variations of flexural rigidity at mountain ranges. *Journal of Geophysical Research*, *102*(B3), 5327–5352.
- Suarez, G., Molnar, P., & Burchfiel, B. C. (1983). Seismicity, fault plane solutions, depth of faulting, and active tectonics of the Andes of Peru, Ecuador, and southern Colombia. *Journal of Geophysical Research*, *88*(B12), 10403–10428.
- Tavera, H., & Buforn, E. (2001). Source mechanism of earthquakes in Peru. *Journal of Seismology*, *5*(4), 519–539.
- Taymaz, T., Jackson, J., & Westaway, R. (1990). Earthquake mechanisms in the Hellenic Trench near Crete. *Geophysical Journal International*, *102*(3), 695–731.
- Thompson, S. C., Weldon, R. J., Rubin, C. M., Abdrakhmatov, K., Molnar, P., & Berger, G. W. (2002). Late Quaternary slip rates across the central Tien Shan, Kyrgyzstan, central Asia. *Journal of Geophysical Research*, *107*(B9), 2203. <https://doi.org/10.1029/2001JB000596>
- Tibaldi, A., & Bonali, L. I. (2018). Contemporary recent extension and compression in the central Andes. *Journal of Structural Geology*, *107*, 73–92.
- Tibaldi, A., Corazzato, C., & Rovida, A. (2009). Miocene-Quaternary structural evolution of the Uyuni-Atacama region, Andes of Chile and Bolivia. *Tectonophysics*, *471*(1–2), 114–135.
- Turcotte, D. L., & Schubert, G. (2002). *Geodynamics*. Cambridge, UK: Cambridge University Press.
- Vega, A., & Buforn, E. (1991). Focal mechanisms of intraplate earthquakes in South America. *Pure and Applied Geophysics*, *136*(4), 449–458.
- Veloza, G., Styron, R., & Taylor, M. (2012). Open-source archive of active faults for northwest South America. *GSA Today*, *22*(10), 4–10.
- Villegas-Lanza, J. C., Chlieh, M., Cavalié, O., Tavera, H., Baby, P., Chire-Chira, J., & Nocquet, J. M. (2016). Active tectonics of Peru: Heterogeneous interseismic coupling along the Nazca megathrust, rigid motion of the Peruvian Sliver, and Subandean shortening accommodation. *Journal of Geophysical Research: Solid Earth*, *121*, 7371–7394. <https://doi.org/10.1002/2016JB013080>
- Ward, K. M., Zandt, G., Beck, S. L., Wagner, L. S., & Tavera, H. (2016). Lithospheric structure beneath the northern Central Andean Plateau from the joint inversion of ambient noise and earthquake-generated surface waves. *Journal of Geophysical Research: Solid Earth*, *121*, 8217–8238. <https://doi.org/10.1002/2016JB013237>
- Watts, A., Lamb, S., Fairhead, J., & Dewey, J. (1995). Lithospheric flexure and bending of the Central Andes. *Earth and Planetary Science Letters*, *134*(1–2), 9–21.
- Wdowinski, S., Oconnell, R. J., & England, P. (1989). A continuum model of continental deformation above subduction zones—Application to the Andes and the Aegean. *Journal of Geophysical Research*, *94*(B8), 10,331–10,346.
- Weber, M. B. I., Tarney, J., Kempton, P. D., & Kent, R. W. (2002). Crustal make-up of the northern Andes: Evidence based on deep crustal xenolith suites, Mercaderes, SW Colombia. *Tectonophysics*, *345*, 49–82.
- Weiss, J. R., Brooks, B. A., Foster, J. H., Bevis, M., Echalar, A., Caccamise, D., et al. (2016). Isolating active orogenic wedge deformation in the southern Subandes of Bolivia. *Journal of Geophysical Research: Solid Earth*, *121*, 6192–6218. <https://doi.org/10.1002/2016JB013145>
- Wells, D. L., & Coppersmith, K. J. (1994). New empirical relationships among magnitude, rupture length, rupture width, rupture area, and surface displacement. *Bulletin of the Seismological Society of America*, *84*(4), 974–1002.
- Wessel, P., Smith, W. H. F., Scharroo, R., Luis, J., & Wobbe, F. (2013). Generic Mapping Tools: Improved version released. *Eos, Transactions American Geophysical Union*, *94*(45), 409–410.
- Whitman, D., Isacks, B. L., Chatelain, J.-L., Chiu, J.-M., & Perez, A. (1992). Attenuation of high-frequency seismic waves beneath the central Andean Plateau. *Journal of Geophysical Research*, *97*(B13), 19,929–19,947.
- Zhou, R., Schoenbohm, L. M., & Cosca, M. (2013). Recent, slow normal and strike-slip faulting in the Pasto Ventura region of the southern Puna Plateau, NW Argentina. *Tectonics*, *32*, 19–33. <https://doi.org/10.1029/2012TC003189>
- Zwicky, P., McCaffrey, R., & Abers, G. (1994). MT5 program.